Article

Cell Reports

FKBP10 Regulates Protein Translation to Sustain Lung Cancer Growth

Graphical Abstract

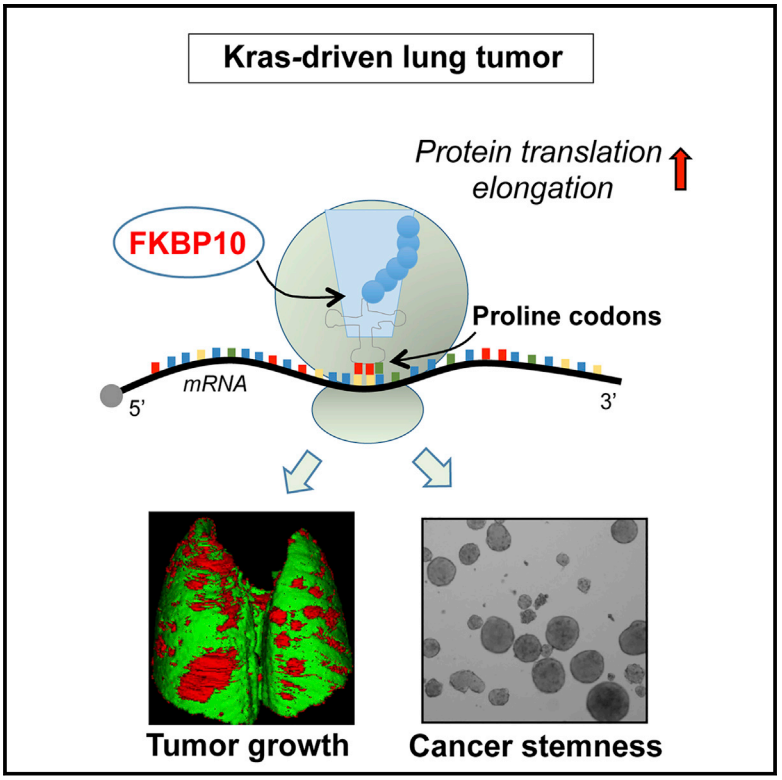

Authors

Giorgio Ramadori, Rafael M. Ioris, Zoltan Villanyi, ..., Pierre Baldi, Martine A. Collart, Roberto Coppari

Correspondence

giorgio.ramadori@unige.ch (G.R.), martine.collart@unige.ch (M.A.C.), roberto.coppari@unige.ch (R.C.)

In Brief

Ramadori et al. show that the peptidyl-prolyl-*cis-trans*-isomerase FKBP10 is selectively expressed in lung cancer cells, and its expression negatively correlates with patient survival. FKBP10 is associated with ribosomes and regulates translation elongation, in particular upon insertion of proline, hence supporting lung cancer growth and stem-like traits.

Highlights

- FKBP10 is selectively expressed in lung cancer cells
- Expression of FKBP10 negatively correlates with survival of lung cancer patients
- FKBP10 downregulation suppresses cancer growth and cancer stem-like features
- FKBP10 regulates translation elongation in particular upon insertion of proline

Ramadori et al., 2020, Cell Reports *30*, 3851–3863
March 17, 2020
https://doi.org/10.1016/j.celrep.2020.02.082

CellPress

Cell Reports
Article

FKBP10 Regulates Protein Translation to Sustain Lung Cancer Growth

Giorgio Ramadori,[1,2,11,*] Rafael M. Ioris,[1,2,11] Zoltan Villanyi,[3,11] Raquel Firnkes,[1,2,11] Olesya O. Panasenko,[1,2,4] George Allen,[3] Georgia Konstantinidou,[5] Ebru Aras,[1,2] Xavier Brenachot,[1,2] Tommasina Biscotti,[6] Anne Charollais,[1,2] Michele Luchetti,[7] Fedor Bezrukov,[8] Alfredo Santinelli,[6] Muntaha Samad,[9,10] Pierre Baldi,[9,10] Martine A. Collart,[3,*] and Roberto Coppari[1,2,12,*]

[1]Department of Cell Physiology and Metabolism, Faculty of Medicine, University of Geneva, 1211 Geneva, Switzerland
[2]Diabetes Center of the Faculty of Medicine, University of Geneva, 1211 Geneva, Switzerland
[3]Department of Microbiology and Molecular Medicine, Institute of Genetics and Genomics, Facutly of Medicine, University of Geneva, 1211 Geneva, Switzerland
[4]Department of Infectious Diseases, Hôpitaux Universitaires de Genève, Genève, Switzerland
[5]Institute of Pharmacology, University of Bern, 3010 Bern, Switzerland
[6]Section of Pathological Anatomy, Department of Biomedical Sciences and Public Health, Università Politecnica delle Marche, 60020 Ancona, Italy
[7]Clinica Medica, Dipartimento di Scienze Cliniche e Molecolari, Università Politecnica delle Marche, 60020 Ancona, Italy
[8]School of Physics and Astronomy, University of Manchester, Oxford Road, Manchester M13 9PL, UK
[9]Department of Computer Science, University of California, Irvine, Irvine, CA 92697, USA
[10]Institute for Genomics and Bioinformatics, University of California, Irvine, Irvine, CA 92697, USA
[11]These authors contributed equally
[12]Lead Contact
*Correspondence: giorgio.ramadori@unige.ch (G.R.), martine.collart@unige.ch (M.A.C.), roberto.coppari@unige.ch (R.C.)
https://doi.org/10.1016/j.celrep.2020.02.082

SUMMARY

Cancer therapy is limited, in part, by lack of specificity. Thus, identifying molecules that are selectively expressed by, and relevant for, cancer cells is of paramount medical importance. Here, we show that peptidyl-prolyl-*cis-trans*-isomerase (PPIase) FK506-binding protein 10 (FKBP10)-positive cells are present in cancer lesions but absent in the healthy parenchyma of human lung. FKBP10 expression negatively correlates with survival of lung cancer patients, and its downregulation causes a dramatic diminution of lung tumor burden in mice. Mechanistically, our results from gain- and loss-of-function assays show that FKBP10 boosts cancer growth and stemness via its PPIase activity. Also, FKBP10 interacts with ribosomes, and its downregulation leads to reduction of translation elongation at the beginning of open reading frames (ORFs), particularly upon insertion of proline residues. Thus, our data unveil FKBP10 as a cancer-selective molecule with a key role in translational reprogramming, stem-like traits, and growth of lung cancer.

INTRODUCTION

A major advance in the fight against cancer is the identification of cancer-specific and cancer-relevant molecular mechanisms. For example, emphasis has been given to the possibility of targeting intracellular (e.g., PI3K) or metabolic (e.g., aerobic glycolysis, fatty acid oxidation) pathways found to be altered in, and important for, cancer cells progression and/or resistance to therapy (Wang and Lippard, 2005; Zugazagoitia et al., 2016). In addition, development of immune checkpoint inhibitors has shown very encouraging efficacy (Iwai et al., 2005; Leach et al., 1996; Son et al., 2017; Wang and Lippard, 2005; Wolchok, 2018; Zugazagoitia et al., 2016). Furthermore, the identification and targeting of cancer stem cells (CSCs) has started to show its potential in humans (Pattabiraman and Weinberg, 2014; Prost et al., 2015). However, cancer relapse and mortality rates are still too high; thus, there is an urgent need for further improvement. Indeed, lack of cancer specificity is a major shortcoming, as it underlies side effects and greatly hinders the effectiveness of current therapy (Wang and Lippard, 2005; Zugazagoitia et al., 2016). For example, current anti-cancer chemotherapy is aimed at reducing proliferation of highly proliferative malignant cells by intravenous delivery of chemical compounds impairing DNA/RNA synthesis and/or microtubule formation (an essential step in cellular division). Unfortunately, these compounds do not target only cancer cells but also affect these functions in normal proliferating cells. Furthermore, CSC-targeting approaches and immune checkpoint inhibitors do not guarantee cancer specificity, and these methods can also lead to serious side effects (Iwai et al., 2005; Leach et al., 1996; Pattabiraman and Weinberg, 2014; Prost et al., 2015; Son et al., 2017; Wang and Lippard, 2005; Wolchok, 2018; Zugazagoitia et al., 2016). The identification of cancer-specific and cancer-relevant molecules is particularly important in the context of lung cancer, which is one of the leading causes of cancer death worldwide and for which there is a clear unmet medical need (Burris, 2009; Camidge et al., 2019; Ferrer et al., 2018; Román et al., 2018). For example, KRAS-mutated non-small cell lung cancer (NSCLC; accounting for ~20% of all lung cancers) (Ferrer et al., 2018; Pao et al., 2005; Román et al., 2018) lacks targeted therapy (Ferrer et al.,

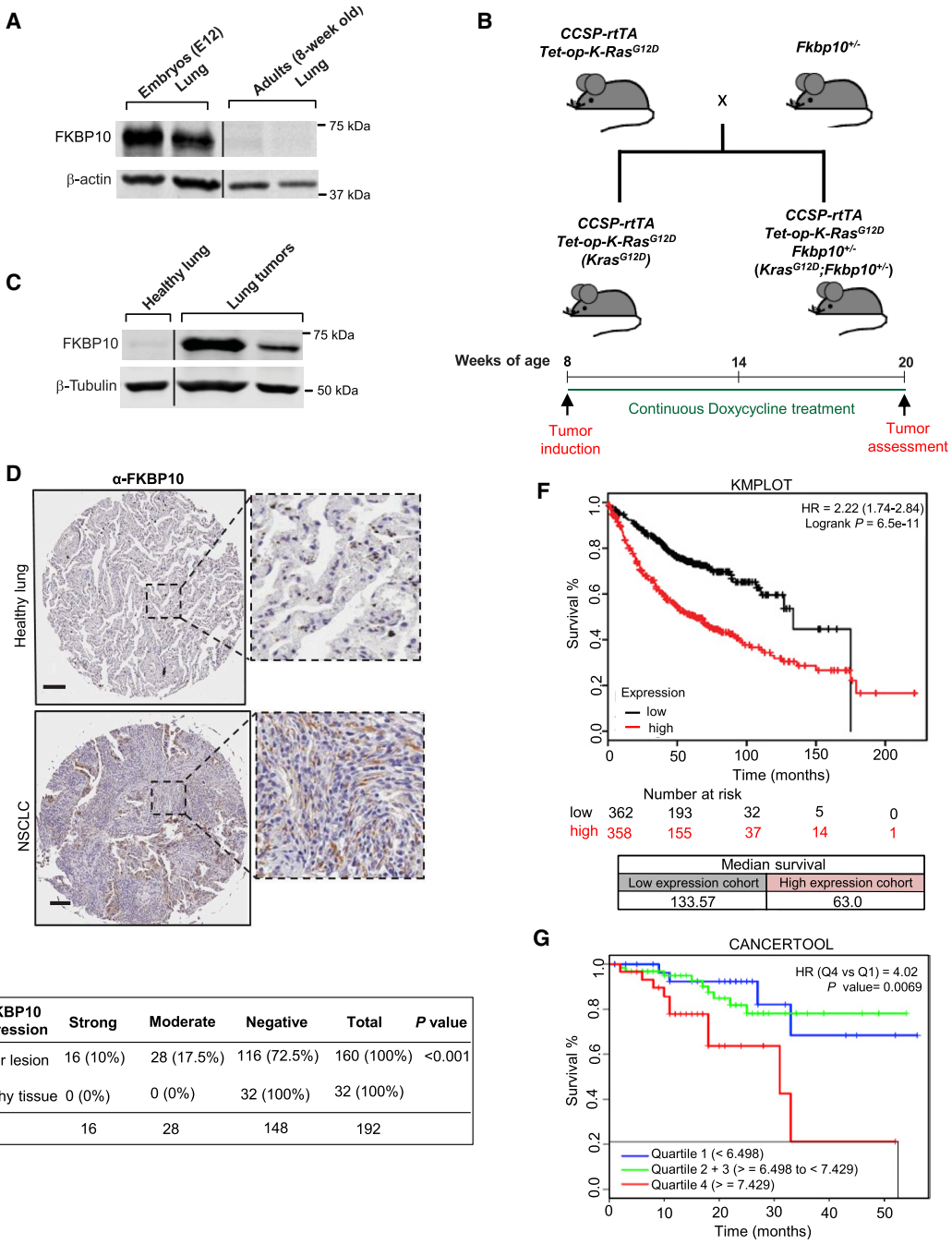

E

FKBP10 Expression	Strong	Moderate	Negative	Total	*P* value
Tumor lesion	16 (10%)	28 (17.5%)	116 (72.5%)	160 (100%)	<0.001
Healthy tissue	0 (0%)	0 (0%)	32 (100%)	32 (100%)	
Total	16	28	148	192	

Figure 1. FKBP10 Is Selectively Expressed by, and Relevant for, Lung Tumors

(A) FKBP10 protein expression in lung tissue of embryos (12th day) and adult mice (8 weeks of age).

(B) Schematic representation of the breeding pairs used to generate *Kras*^{G12D}; *Fkbp10* haploinsufficiency mice model and experimental timeline of this mouse model.

(C) Immunoblot showing expression of FKBP10 in healthy lung and lung tumors of *Kras*^{G12D} mice.

(D) Representative images of human lung tumor and healthy lung tissue stained against FKBP10 (positive staining is shown in brown color). Scale bar: 50 μm.

(E) Number of cases and percentage of FKBP10 positive (strong expression, >25% of FKBP10-positive cells; moderate expression, <25% of FKBP10-positive cells) and negative expression in human healthy and tumor lung tissues.

(F and G) FKBP10 expression negatively correlates with survival of patients with lung adenocarcinoma. Data were obtained from KMPLOT (high and low values of expression were split by median expression of FKBP10) (F) and CANCERTOOL database (G). Quartiles represent ranges of expression that divide the set of values into quarters. Quartile color code: blue, Q1; green, Q2 + Q3; red, Q4. Each quartile includes 32 patients.

(legend continued on next page)

2018; Pao et al., 2005; Román et al., 2018) and is associated with poor outcome (Ferrer et al., 2018; Román et al., 2018).

Several proteins are highly expressed during organismal development, while their expression becomes low or negligible in most tissues during adulthood. However, a few of these proteins are re-expressed at high level in cancer lesions (Monk and Holding, 2001), where they might contribute to tumorigenesis. Pertinent to lung cancer, these include carcinoembryonic antigen (Cortazar et al., 2018), Mucin-1, melanoma-associated antigen (MAGE-3), 5T4 tumor antigen, and sal-like protein 4 (SALL4) (Boghaert et al., 2008; Yasumoto et al., 2009; Yong et al., 2016). Unraveling proteins that are relevant for, and selectively expressed by, tumors is of paramount medical interest, as it may pave the way for better cancer diagnostic and therapeutic approaches. In fact, targeting proteins that are selectively expressed by cancer cells is a promising avenue to specifically hinder cancer growth while sparing healthy tissue. To this end, we have previously reported that FK506-binding protein 10 (FKBP10), an endoplasmic reticulum (ER) chaperone containing four peptidyl-prolyl-*cis-trans*-isomerase (PPIase) domains (Chen et al., 2017; Ishikawa et al., 2008), might have NSCLC-relevant attributes (Ramadori et al., 2015). FKBP10 is highly expressed during development, and its expression decays in adulthood (Patterson et al., 2000). During organismal growth, FKBP10 is important for bone development. Indeed, inborn loss-of-function mutations in FKBP10 have been associated with the pathogenesis of osteogenesis imperfecta and Bruck syndrome (Alanay et al., 2010; Christiansen et al., 2010; Kelley et al., 2011). Pertinent to cancer, in addition to our published results on NSCLC (Ramadori et al., 2015), FKBP10 has also been detected in human colorectal adenocarcinoma and gastric cancer but not in healthy colorectal and gastric tissues (Liang et al., 2019; Olesen et al., 2005). Other reports further indicate an oncogenic role of FKBP10. For example, in renal cell carcinoma, FKBP10 is overexpressed, and its downregulation diminished cell proliferation, invasion, and migration (Ge et al., 2017). Yet others have shown that reduced FKBP10 expression correlates with poorer overall survival of patients with high-grade ovarian serous carcinoma (Quinn et al., 2013). Thus, although FKBP10 expression appears to be restricted within the cancer lesion in adulthood, its role in cancer still needs to be fully understood.

Here, we combined *in vivo* and *in vitro* functional approaches to establish the specificity and relevance of FKBP10 in KRAS-driven NSCLC and unravel, at least in part, the mechanism underlying its pro-tumoral effect in this subset of lung cancer for which there is a clear unmet medical need.

RESULTS

FKBP10 Is Selectively Expressed by, and Relevant for, Lung Tumors

To determine whether FKBP10 is restrictedly expressed in lung cancer, we first ruled out the possibility that FKBP10 is expressed in the healthy lung in adulthood. Indeed, our data shown in Figure 1A are in keeping with previously published results (Patterson et al., 2000) indicating that FKBP10 is highly expressed in lung during the fetal stage, whereas its content decays in adulthood. Next, we generated a genetically engineered mouse that develops KRAS-driven lung tumors (i.e., $Kras^{G12D}$ mice). This is an established murine model of human KRAS-mutated NSCLC, a type of cancer accounting for ~20% of all lung cancers (Ferrer et al., 2018; Fisher et al., 2001; Pao et al., 2005; Román et al., 2018). $Kras^{G12D}$ mice were obtained by breeding a transgene encoding $Kras^{G12D}$ under the control of the tetracycline operator (*Tet-op-Kras*) to a transgene expressing the reverse tetracycline transactivator in the respiratory epithelium under the control of the Clara cell secretory protein promoter (*CCSP-rtTA*) (Figure 1B). The resulting bi-transgenic $Kras^{G12D}$ mice develop lung tumors with 100% penetrance following continuous doxycycline (doxy) administration (Fisher et al., 2001). Our data shown in Figure 1C confirm that FKBP10 is not expressed in the healthy lung, while its content is promptly detectable in tumor lesions of $Kras^{G12D}$ mice. To expand our analysis to human, we performed FKBP10 immunohistochemistry (IHC) analysis in 32 cases of healthy lung tissue and 160 cases of NSCLC (80 cases of each squamous cell carcinoma and adenocarcinoma). FKBP10-positive cells were detected only in cancer lesions and not in the healthy parenchyma (Figures 1D and 1E; Tables S1 and S2). These data demonstrate that in the murine and human adult lung FKBP10 expression is cancer specific.

To investigate the relevance of FKBP10 in human cancer, we probed FKBP10 in KMPLOT (Nagy et al., 2018) and CANCERTOOL (Cortazar et al., 2018) (these public databases catalog the correlation between patient survival and the expression of individual genes in several types of cancer, including lung cancer). Of note, we found that expression of FKBP10 inversely correlates with the survival of patients affected by lung adenocarcinoma (Figures 1F and 1G). Notably, high expression of FKBP10 reduces patients' survival probability by more than 50% compared with the low FKBP10 expression cohort, an effect seen in both genders (Figures 1F and S1A). Further analysis of the CANCERTOOL database revealed that the expression of FKBP10 is similar between lung tumors bearing mutant KRAS, EGFR, and KRAS/EGFR non-mutants (Figure S1B), suggesting that the relevance of FKBP10 in lung cancer is wide ranging (i.e., it is not limited to a specific genotype). Last, we found that the expression of FKBP10 inversely correlates with patients' survival in several other cancer-type cohorts (Figure S1C), hence broadening the putative relevance of FKBP10 in human cancer.

FKBP10 Downregulation before Tumor Onset Hinders Kras-Driven Lung Tumorigenesis

To directly test the significance of FKBP10 in tumorigenesis *in vivo*, we assessed the outcome of FKBP10 downregulation in tumors of $Kras^{G12D}$ mice. Because whole-body FKBP10 deficiency is embryonically lethal (Lietman et al., 2014), we generated $Kras^{G12D}$ mice heterozygous for a *Fkbp10*-knockout allele ($Kras^{G12D}$; $Fkbp10^{+/-}$) and their controls ($Kras^{G12D}$) by breeding the *Tet-op-Kras*, *CCSP-rtTA*, and *Fkbp10*-knockout alleles as

Data were analyzed by contingency table using Fisher's exact test (E) to determine the association between positive (strong and moderate expression) and negative FKBP10 expression in tumor lesions compared with healthy lung tissue; $p < 0.001$.
See also Figure S1 and Tables S1 and S2.

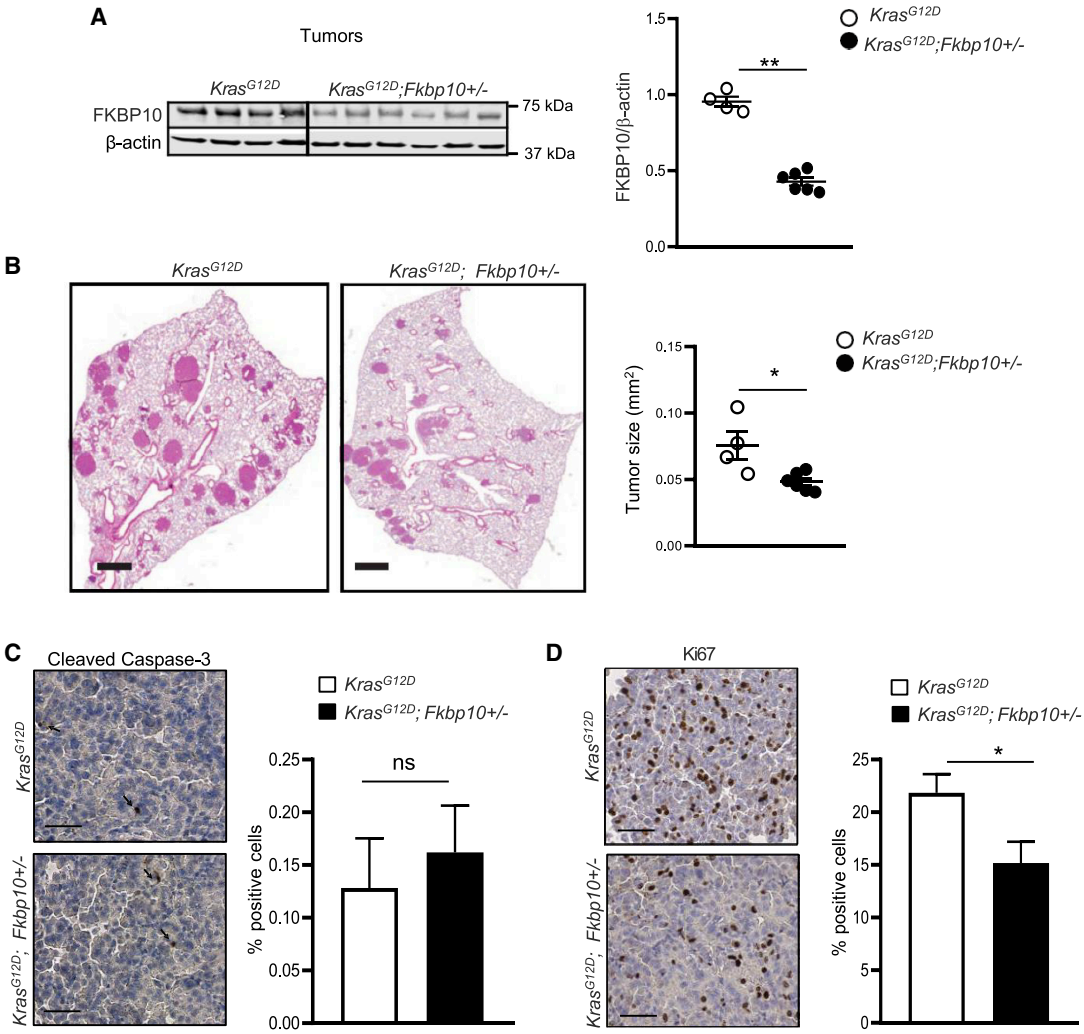

Figure 2. FKBP10 Downregulation Hinders Kras-Driven Lung Tumorigenesis

(A) Immunoblot showing expression of FKBP10 in lung tumors and scatterplot showing relative quantification of FKBP10 protein content (normalization over β-actin).

(B) Representative images of lung sections stained with hematoxylin and eosin and scatterplot showing quantification of tumor size (mm^2).

(C) Representative images of lung sections stained for apoptosis (anti-cleaved caspase-3) and histogram indicating percentage of apoptotic positive cells/tumor cells. Arrows indicate cleaved caspase-3-positive cells.

(D) Representative images of lung sections stained for proliferation (anti-Ki67) and histogram indicating percentage of proliferative positive cells/tumor cells.

Data are shown as mean ± SEM. Statistical analyses were done using two-tailed unpaired Student's t test (A–D); *$p < 0.05$ and **$p < 0.01$. Scale bars: 1 mm (B) and 50 μm (C and D); n = 4–6 mice per group (A–D).

indicated in Figure 1B. These mice were then treated with doxy for 12 weeks, starting at 8 weeks of age (Figure 1B). Endpoint analysis of the lungs revealed that FKBP10 haploinsufficiency results in approximately 50% reduction of FKBP10 protein level in lung tumors (Figure 2A). Strikingly, tumor burden was found to be reduced by about 40% in *Kras*^{G12D}; *Fkbp10*$^{+/-}$ mice compared with *Kras*^{G12D} controls (Figure 2B). Changes in tumor growth could be due to increased cell death and/or decreased cell proliferation. Notably, although the status of apoptosis level (assessed using IHC against cleaved caspase-3) was unchanged (Figure 2C), cell proliferation (assessed using IHC against Ki67) was significantly reduced in tumors of *Kras*^{G12D}; *Fkbp10*$^{+/-}$ mice compared with controls (Figure 2D). Collectively, our findings establish that reduced FKBP10 expression before tumor onset hinders Kras-driven lung tumorigenesis.

FKBP10 Downregulation after Tumor Onset Suppresses Kras-Driven Lung Tumorigenesis

To further test whether FKBP10 downregulation is of anti-cancer value, we generated an additional mouse model in which *Fkbp10* can be deleted conditionally. This animal model bears five different alleles: *Tet-op-Kras* (Konstantinidou et al., 2013),

CCSP-rtTA (Konstantinidou et al., 2013), two *lox-P*-flanked *Fkbp10* loci (Fisher et al., 2001), and the *Ubi-Cre* (Ruzankina et al., 2007) allele (*Kras*^{G12D}; *Fkbp10*$^{loxP/loxP}$; *Ubi-Cre* [KFU]) (Figure S2A). By delivering doxy and tamoxifen, this mutant mouse allows time-dependent induction of tumorigenesis and *Fkbp10* deletion, respectively. As indicated in Figure 3A, we triggered tumorigenesis at 8 weeks of age and *Fkbp10* deletion post-tumor onset at 14 weeks of age. Endpoint analysis of the lungs and tumors of KFU mice showed an approximate 85% reduction of FKBP10 protein content compared with controls (*Kras*^{G12D}; *Fkbp10*$^{loxP/loxP}$ [KF]) that similarly underwent doxy and tamoxifen treatments (Figure 3B). Histological analysis revealed a dramatic reduction of tumor area in KFU compared with KF mice (Figure 3C). Additionally, to determine *in vivo* tumor growth dynamics, X-ray micro-computed tomography (micro-CT) scanning was performed at weeks 0, 6, and 12 after tumorigenesis induction. At week 6, both cohorts presented no difference in tumor volume (Figure 3D). Importantly, although tumor volume continued to increase in controls, it strikingly decreased in KFU mice (Figures 3D and S2B). These results are in line with data shown in Figure 3C indicating that FKBP10 downregulation after tumor onset greatly reduces tumor burden in a KRAS-driven NSCLC mouse model. We next examined whether increased apoptosis and/or decreased proliferation could explain the dampening of tumor burden. Remarkably, using IHC against cleaved caspase-3, we found a 3-fold increase in apoptosis levels in KFU mice compared with KF controls (Figure 3E), whereas no change in proliferation (IHC against Ki67) was observed between genotypes (Figure 3F). Together, these data demonstrate that *Fkbp10* deletion after tumor onset nearly abolishes tumor burden in mice, hence suggesting FKBP10 as a target of therapeutic potential against KRAS-driven NSCLC.

FKBP10 Promotes Cancer Stem-like Traits via Its PPIase Activity

The aforementioned data establish that FKBP10 downregulation suppresses tumor burden. Yet a smaller lesion does not equal a less dangerous tumor, as it might be enriched in CSCs (a subpopulation of cells with high tumorigenic and self-renewal capacity) (Ioris et al., 2017; Lapidot et al., 1994; Pattabiraman and Weinberg, 2014; Wang and Dick, 2005). Thus, we aimed to assess whether FKBP10 affects cancer stemness. First, the ability of cancer cells to form spheres in non-adherent *in vitro* cultures is a well-established readout of CSCs (Dontu et al., 2003; Ioris et al., 2017; Ponti et al., 2005; Rasheed et al., 2010). Hence, we assessed the capacity of human lung (H1650 and A549), colorectal (DLD-1 and HT-29), and breast (MCF10DCIS) cancer cell lines transduced with a control vector (empty vector) compared with cells transduced with a vector containing short hairpin RNA (shRNA) against FKBP10 (shFKBP10; leading to FKBP10 downregulation) to form tumorspheres. Our results indicate that FKBP10 downregulation significantly decreased tumorsphere-forming capacity of the aforementioned cancer cells (Figures 4A and S3A). Second, we assessed the percentage of the cell population displaying high aldehyde dehydrogenase (ALDH) activity, which has been shown as a CSC marker in certain tumors, including lung, colon, and breast cancers (Carpentino et al., 2009; Cheung et al., 2007; Ginestier et al., 2007; Ioris et al., 2017). Of note, FKBP10 downregulation diminished the percentage of cancer cells with high ALDH activity (ALDH^{high}) (Figure 4B). Next, by fluorescence-activated cell sorting, we isolated A549 cells with high and low ALDH activity (ALDH^{low}). Remarkably, ALDH^{high} A549 cells harboring empty vector or shFKBP10 were enriched in CSCs, as their tumorsphere-forming capacity was higher compared with their ALDH^{low} controls (Figure S3B). Of note, ALDH^{high} A549 cells harboring empty vector gave rise to a larger number of tumorspheres compared with ALDH^{high} A549 cells harboring shFKBP10 (Figure S3B); these data underscore the importance of FKBP10 in maintaining the CSCs phenotype.

A reduced number of CSCs should lead to reduced tumorigenic capacity *in vivo*. Thus, we tested whether FKBP10 downregulation delays the appearance of A549 and H1650 xenografts. These cells, with or without FKBP10 downregulation, were injected into the flank of non-obese diabetic/severe combined immunodeficient (NOD/SCID) mice, and their growth was monitored over time. Results shown in Figures 4C and S3C demonstrate that FKBP10 downregulation significantly delays appearance of these tumor xenografts. Next, we performed gain-of-function experiments and found that FKBP10 overexpression (FKBP10 ove) significantly increases the tumorsphere-forming capacity of human cancer cells (Figure 4D). To further determine the mechanism underlying the pro-CSC action of FKBP10, we directly tested the relevance of its PPIase activity. By overexpressing a mutant FKBP10 (FKBP10 8FY, which contains mutations in all four PPIase domains; Chen et al., 2017), we uncovered that the PPIase activity of FKBP10 is required for its pro-tumorsphere-forming action. Indeed, although FKBP10 8FY was similarly overexpressed as wild-type FKBP10, it did not change the tumorsphere-forming capacity of these cancer cells (Figure 4D). Collectively, our data indicate that FKBP10 promotes the stemness and tumorigenic capacity of human cancer cells through a mechanism dependent on its PPIase activity.

FKBP10 Regulates Translation Elongation

Altogether, the aforementioned results indicate that FKBP10 is a cancer-specific and cancer-relevant molecule. Thus, to determine the mechanism underlying its role in cancer, we performed an unbiased experiment aimed at identifying FKBP10 interacting proteins. Analysis by liquid chromatography (LC)-mass spectrometry (MS) of A549 cell lysates obtained after protein immunoprecipitation (IP) with a specific antibody against FKBP10 (Figure S4A) revealed a list of 146 putative interacting partners (Table S3). Gene Ontology (Ashburner et al., 2000; The Gene Ontology Consortium, 2019) analysis of this list showed a significant enrichment of proteins representing structural constituents of ribosomes (Figure 5A). These proteins obtained by IP were enriched in A549 cancer cells with intact versus reduced FKBP10 expression (Figure S4A). To test whether FKBP10 interacts with ribosomes, A549 cell lysates were separated on a sucrose gradient (Faller et al., 2015; Liu et al., 2013). Indeed, FKBP10 was detected in the ribosome-containing fractions, particularly in monosome and light polysome fractions (Figure 5B). To assess the functional relevance of this association, we measured [35S]-methionine incorporation in A549 cells with or without FKBP10 knockdown. FKBP10 knockdown reduced protein

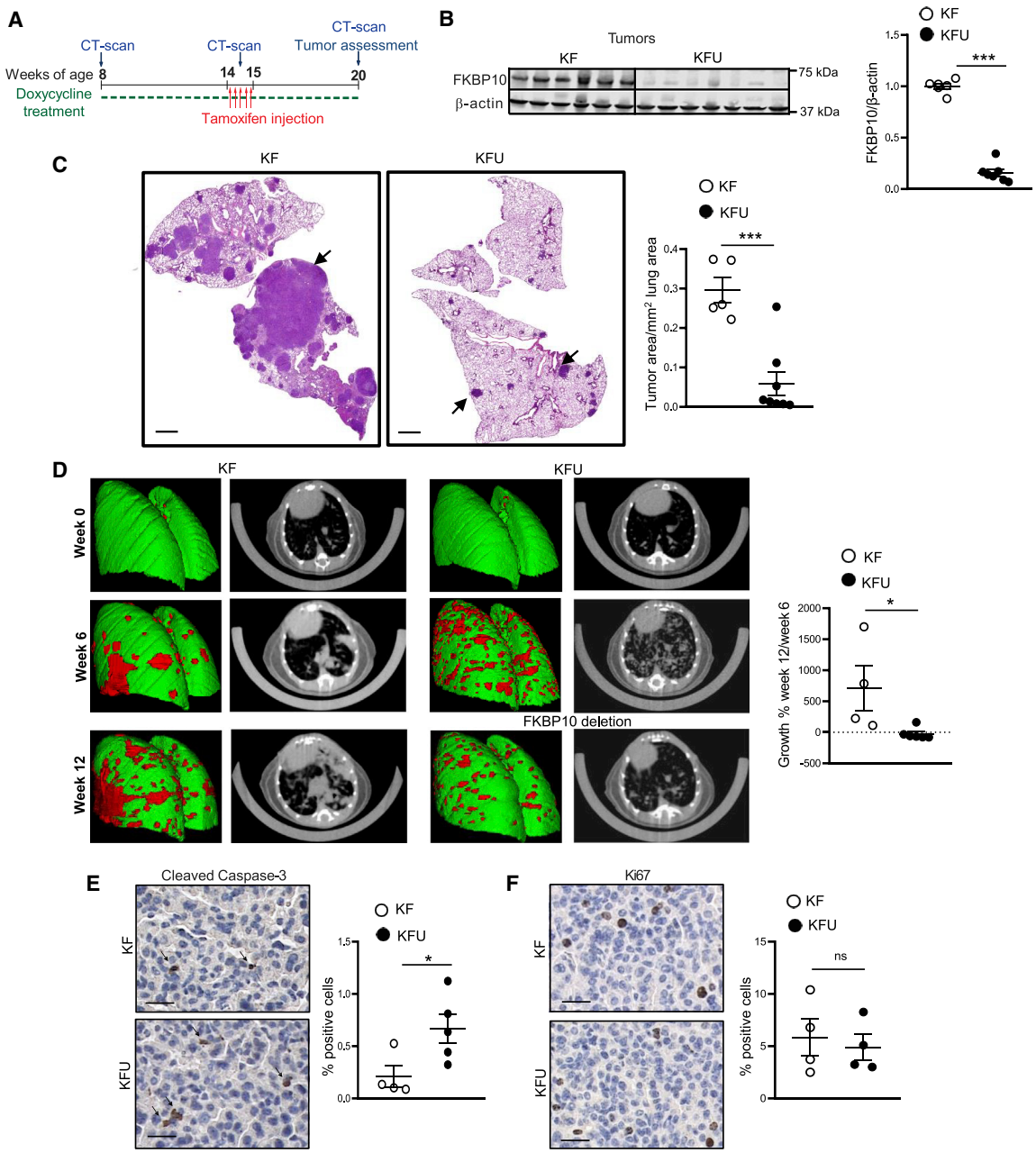

Figure 3. FKBP10 Ablation Suppresses Tumorigenesis after Tumor Onset

(A) Experimental timeline of *Kras*^{G12D}; *Fkbp10*$^{loxP/loxP}$ (KF) and *Kras*^{G12D}; *Fkbp10*$^{loxP/loxP}$; *Ubi-Cre* (KFU) mouse models.

(B) Immunoblot showing expression of FKBP10 in lung tumors and scatterplot showing quantification of FKBP10 protein content (normalization over β-actin).

(C) Representative images of lung sections stained with hematoxylin and eosin and scatterplot showing quantification of tumor size (tumor area per mm^2 of lung area). Arrows indicate tumors.

(D) Representative images showing three-dimensional (3D) lung (green) and tumors/vessels (red) renderings dorsally and axial sections of thoracic cavity at the indicated time points of two individual mice (KF and KFU). Scatterplot illustrating the percentage tumor growth of week 12 divided by week 6.

(E) Representative images of lung sections stained for apoptosis (anti-cleaved caspase-3) and scatterplot indicating percentage of apoptotic positive cells/tumor cells. Arrows indicate cleaved caspase-3-positive cells.

(F) Representative images of lung sections stained for proliferation (anti-Ki67) and scatterplot indicating percentage of proliferative positive cells/tumor cells.

Data are represented as mean ± SEM. Statistical analyses were done using two-tailed unpaired Student's t test (B–F); *$p < 0.05$ and ***$p < 0.001$. Scale bars: 1 mm (C) and 50 μm (E and F); n = 4–8 mice per group (B–F).

See also Figure S2.

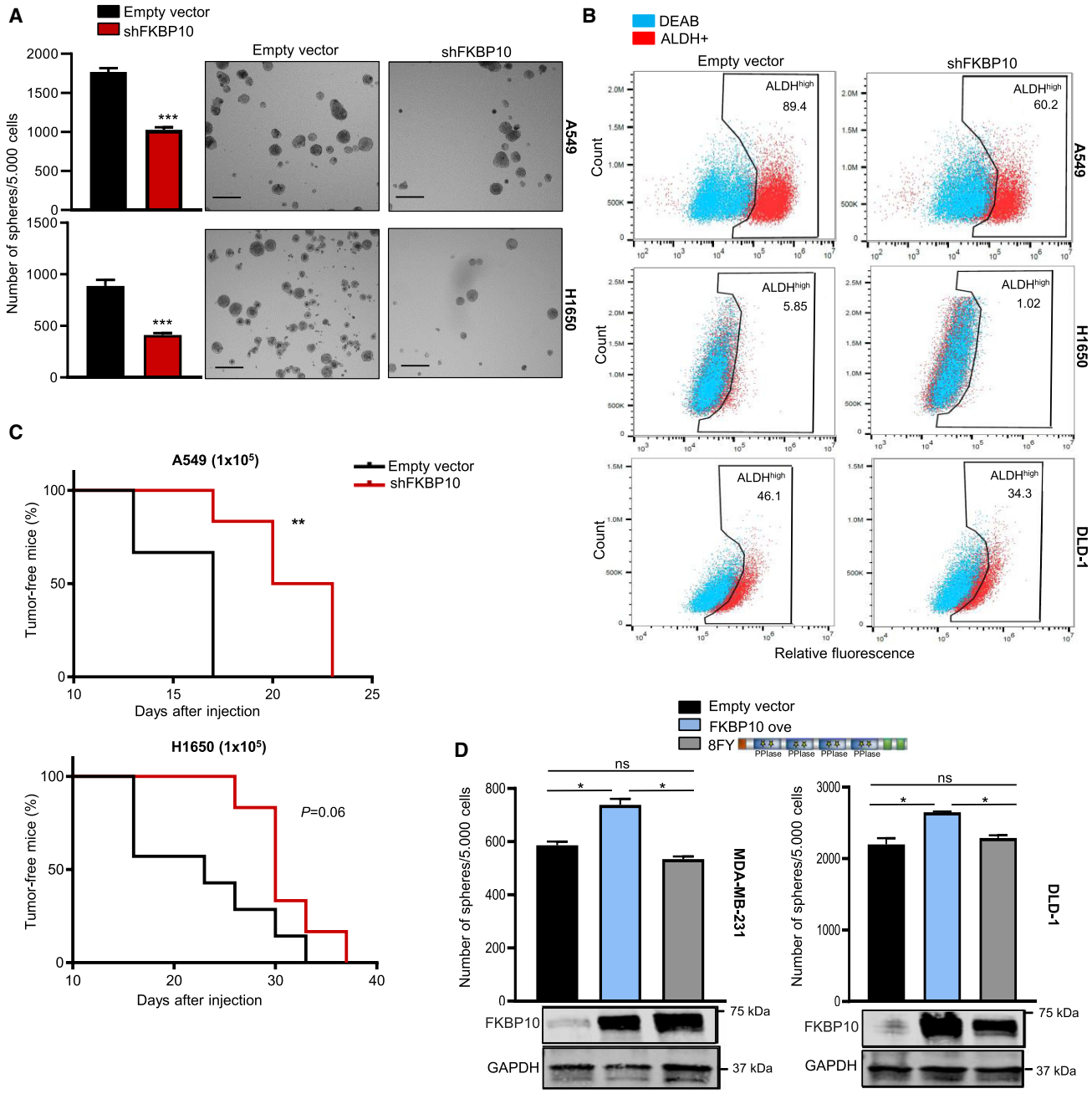

Figure 4. FKBP10 Promotes Cancer Stem-like Traits via Its PPIase Activity

(A) Tumorsphere formation capacity of A549 and H1650 lung cancer cells harboring empty vector or shFKBP10. Scale bar: 50 μm.

(B) ALDH activity of A549, H1650, and DLD-1 cells harboring empty vector or shFKBP10. ALDH, aldehyde dehydrogenase; DEAB, N,N-diethylaminobenzaldehyde.

(C) Kaplan-Meier curves comparing percentage of tumor-free mice at different time points after subcutaneous injection of A549 and H1650 cells harboring empty vector or shFKBP10 (at concentration of 1 × 10^5 cells). n = 6 mice per group.

(D) Tumorsphere formation capacity of MDA-MB-321 and DLD1 cells harboring empty vector, a vector overexpressing FKBP10, or FKBP10 mutant (8FY) (mutations in all four PPIase domains of the protein). Below bars are shown western blot data revealing molecular weight (right lanes) and FKBP10 and GAPDH protein content.

Data are shown as mean ± SEM. Comparisons were performed using two-tailed unpaired Student's t test (A and D) or log-rank test (C); *p < 0.05, **p < 0.01, and ***p < 0.001.

See also Figure S3.

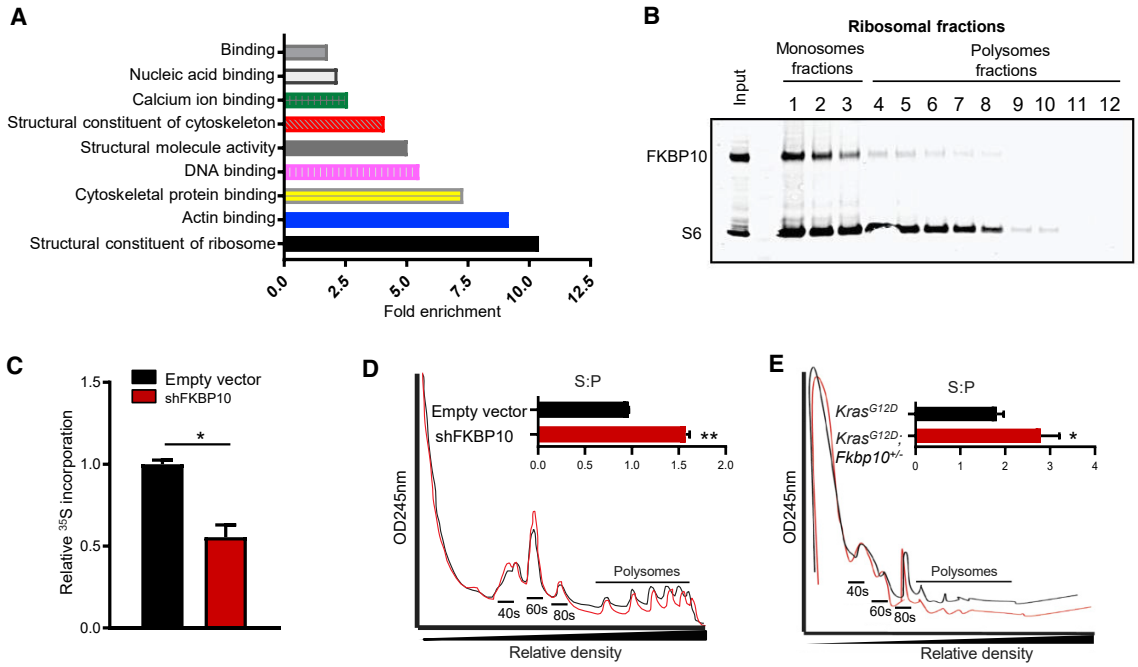

Figure 5. FKBP10 Interacts with Ribosomes

(A) Gene Ontology (Ashburner et al., 2000; The Gene Ontology Consortium, 2019) enrichment analysis was done from a list of proteins obtained by LC-MS detection in A549 cell lysate previously immunoprecipitated with a FKBP10 antibody.

(B) Total cellular extracts were separated on a 7%–47% sucrose gradient and the fractions were analyzed by western blot for the levels of FKBP10 and the ribosomal S6 protein as a control for the ribosome-containing fractions.

(C) Translation was assessed by [35S]-methionine incorporation in A549 cells harboring empty vector or a vector containing shRNA against FKBP10 leading to FKBP10 downregulation (shFKBP10).

(D) Representative polysome profiles of A549 cells with or without knockdown of FKBP10 and histograms showing relative ratio between sub-polysome and polysome fractions (S:P).

(E) Representative polysome profiles from tumors of $Kras^{G12D}$ and $Kras^{G12D}$; $Fkbp10^{+/-}$ mice with histograms as in (D).

Data are represented as mean ± SEM. Statistical analyses were done using two-tailed unpaired Student's t test (C–E); *p < 0.05 and **p < 0.01.

See also Figure S4 and Table S3.

translation by half (Figure 5C). Thus, these results suggest that FKBP10 regulates protein translation.

To further evaluate this observation, we assessed polysome profiles *in vitro* and *in vivo*. Separation of A549 lysates on a sucrose gradient (Faller et al., 2015; Liu et al., 2013) showed that FKBP10 knockdown causes a concomitant decrease in polysome and increase in monosome levels (Figure 5D). A similar reduction in polysome levels was observed in lung tumors of $Kras^{G12D}$; $Fkbp10^{+/-}$ mice compared with their FKBP10-intact $Kras^{G12D}$ mice (Figure 5E). Such changes in polysome profiles are consistent with differences in protein translation elongation. Nevertheless, because FKBP10 has been reported to function as an ER chaperone (Chen et al., 2017; Ishikawa et al., 2008), its knockdown could cause attenuation of translation initiation due to proteotoxic stress (Liu et al., 2013). Thus, we assessed the level of phosphorylation of the eukaryotic translation initiation factor 2 α (p-eIF2α; a prominent event of the unfolded protein response upon ER stress aimed at inhibiting protein translation initiation; Guan et al., 2014) in A549 cells and in tumors. Our data indicated no changes in p-eIF2α level upon FKBP10 knockdown in A549 cells (Figure S4B) or in tumor samples from $Kras^{G12D}$; $Fkbp10^{+/-}$ mice compared with their $Kras^{G12D}$ controls (Figure S4C). Furthermore, the formation of stress granules, an established readout of translation initiation arrest (Liu et al., 2013), was not affected by FKBP10 downregulation in A549 cells (Figure S4D).

To investigate how FKBP10 affects translation elongation, we performed ribosome profiling (Ribo-seq) of A549 cells harboring empty vector or shFKBP10 (Figures S5A–S5C; Tables S4 and S5). At a global level, relatively similar amounts of mRNAs had a higher or a lower density of ribosomes upon FKBP10 knockdown, irrespective to whether they were of high or low expression, respectively (Figure 6A; Table S5). Because FKBP10 has PPIase activity, consisting in *cis-trans* isomerization of peptides bound with the amino acid proline, we investigated whether mRNAs with higher proline content were more likely to show changes in ribosome profiles upon FKBP10 knockdown. However, there was no correlation (Figure S5D). We questioned whether generally ribosomes might tend to pause longer on proline codons (P-site footprint accumulation); nevertheless, there was no general codon bias change upon FKBP10 knockdown (Figure S5E). Metagene analysis revealed that the lung cancer cells have low reads at the beginning of open reading frames (ORFs) and that these are increased upon FKBP10 knockdown,

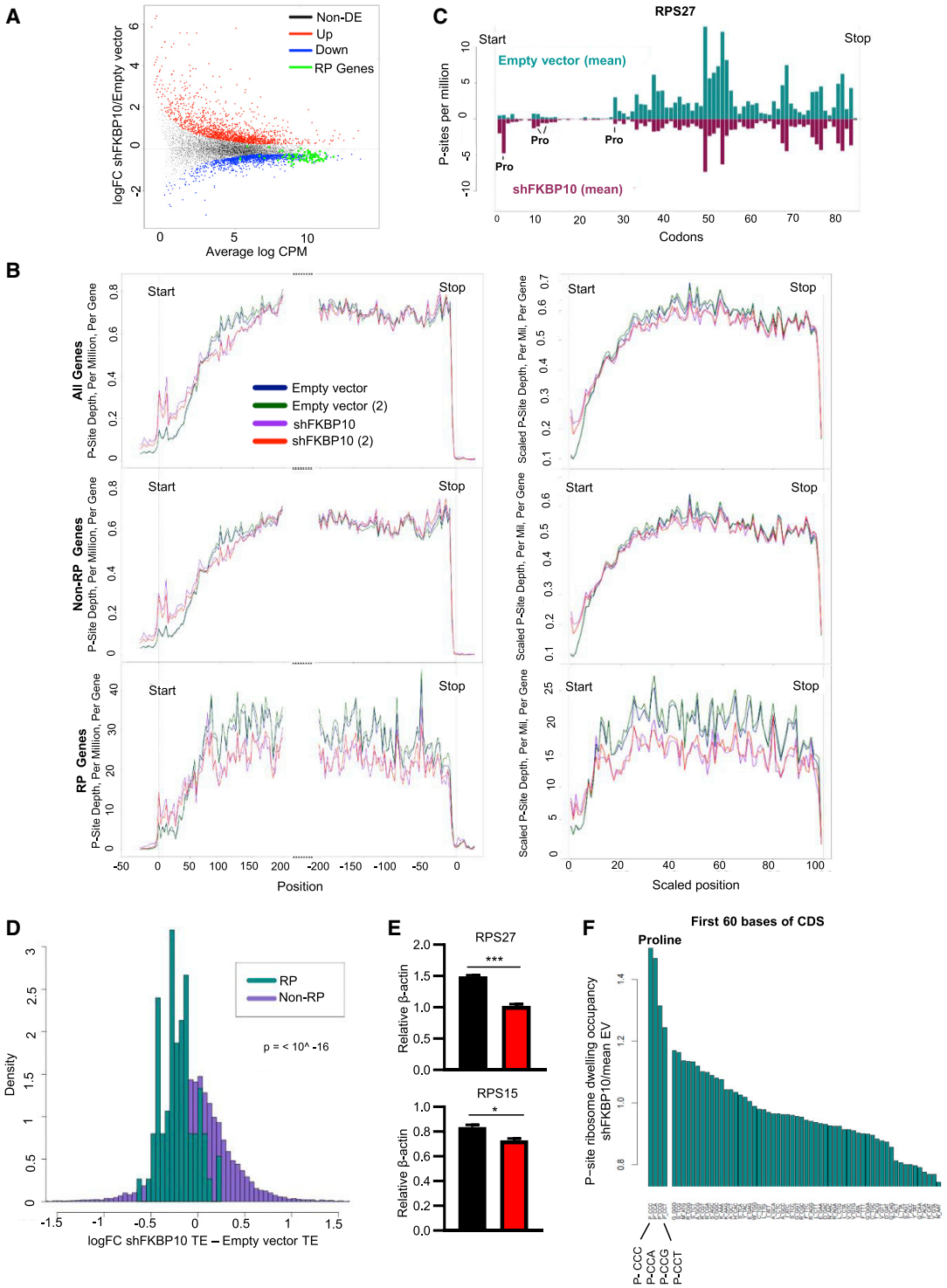

Figure 6. FKBP10 Regulates Translation Elongation

(A) All fold changes generated by edgeR differential expression analysis comparing P-site counts for each CDS in A549 cells harboring an empty vector and shFKBP10 (duplicates) were plotted against counts per million. Significantly upregulated genes overlaid in red, downregulated in blue, and RP genes are highlighted in green.

(B) Ribosome profiles were obtained from A549 harboring an empty vector or shFKBP10 in duplicates. Left: for three gene sets (all genes, non-RP genes, and RP genes), the ribosome footprint P-site counts located in the first and last 201 bases of each CDS were aggregated and normalized to gene number and total P-site

(legend continued on next page)

with an inversion approximately 50–100 nt downstream of the start (Figure 6B, upper panel). The impact of FKBP10 manipulation on the early stage of translation elongation is consistent with the observation that FKBP10 is detected mostly in monosomes and light polysomes rather than in heavy polysomes (Figure 5B).

As translation of ribosomal protein (RP) mRNAs contributes importantly to the global level of translation in cells dividing rapidly, we determined the contribution of RP mRNAs to these metagene profiles. The increased reads at the beginning of ORFs with an inversion between 50 and 100 nt was observed similarly for all mRNAs, non-RP mRNAs, and RP mRNAs (Figure 6B). Instead, the reduced reads at the end of ORFs in the FKBP10-knockdown group was found on the metagene of RP mRNAs (Figure 6B, lower panel) and mostly not of non-RP mRNAs (Figure 6B, middle panel). These results indicate that FKBP10 knockdown has a qualitative impact on translation elongation, leading to a genome-wide increase of ribosomes at the beginning of ORFs and a specific depletion of ribosomes on RP mRNAs starting approximately 100 nt from start (Table S5).

To determine whether the effect of FKBP10 downregulation on RP mRNAs was due to an impact on their translatability rather than on the total levels of RP mRNAs, we performed RNA sequencing (RNA-seq) of A549 cells harboring empty vector or shFKBP10 (Figure S6A; Tables S4 and S5). Overall, the level of the vast majority of RP mRNAs was not significantly different between control and FKBP10-knockdown cells (Figure S6B). For selected RP mRNAs (Figure S6B), the RNA-seq results were confirmed by quantitative real-time polymerase chain reaction (Figure S6C). RPS27 is a typical example of a RP whose mRNA level was unchanged (Figures S6B and S6C) while displaying a differential Ribo-seq pattern: FKBP10 downregulation led to a clear ribosome accumulation at the beginning and a reduction at the end of the RPS27 ORF in A549 cells (Figure 6C).

We then expressed translation of mRNAs (average density of ribosomes on the mRNA per kilobase per total counts [RPKM]) to the level of the mRNA in the total mRNA pool (Figures 6D and S6D; Table S6) (translatability). Translatability of RP mRNAs was reduced upon FKBP10 knockdown (Figure 6D, green bars; Figure S6D, green dots). To further test whether reduced translatability affected total RP levels, using western blot assay we measured the protein contents of RP species that displayed lowest translatability (Figure 6D; e.g., RPS15 and RPS27). Although the mRNA levels of these RPs were normal (Figure S6B), their protein contents were reduced in A549 cells with FKBP10 knockdown compared with controls (Figures 6E and S6E). Taken together these results indicate that FKBP10 downregulation affects translation elongation, increasing ribosome pausing at the beginning of the ORFs, leading specifically to a general reduction of RP mRNA translation.

To understand the genome-wide impact of FKBP10 for translation elongation at the beginning of ORFs (e.g., the first 60 nt downstream of the AUG), we evaluated whether the increased reads upon FKBP10 knockdown were similarly distributed on all codons. Strikingly, upon FKBP10 knockdown, P-site occupancy increased most on the four proline codons compared with any other codon (Figure 6F). This suggests that FKBP10 promotes translation elongation after insertion of prolines to the nascent chain, specifically early during translation elongation (see model in Figure S6F). These data additionally indicate that slower elongation at the beginning of the ORFs is detrimental in particular for translation of RP mRNAs (Figures 6B, 6D, and S6D).

DISCUSSION

Cancer cells reprogram protein translation to support their malignant phenotype. Accordingly, several oncogenic mutations (e.g., oncogenic activation of MYC, KRAS, and PIK3CA) and/or loss of function of tumor suppressors (e.g., PTEN and P53) lead to dysregulation of the protein synthesis rate (Bhat et al., 2015). Moreover, production of ribosomes has been shown to support cancer growth (Penzo et al., 2019). However, cancer-specific molecular mechanisms regulating these translational processes are unknown. Our results support the notion that FKBP10 is an adaptive mechanism required for the increased protein synthesis demand (e.g., RP production) in proliferating cancer cells. Furthermore, our study suggests that FKBP10 is required for protein translation in cancer cells by its PPIase activity (consisting of *cis-trans* isomerization of nascent peptides bound with the amino acid proline) and thus accelerates translation elongation, in particular upon insertion of proline codons. This is important in light of recent work indicating a strong dependence on proline availability for translation elongation by cancer cells (Loayza-Puch et al., 2016; Sahu et al., 2016). Yet to the best of our knowledge, it has never been described that isomerization of proline at an early phase of translation elongation could be a limiting event for tumor growth.

An interesting aspect of our findings relates to the role of the PPIase activity. Indeed, our data indicate that this enzymatic

occupancy of all coding regions for each sample. Right: for the same gene sets, each CDS was split into 100 equal-length bins, and the number of P-site counts located in each was aggregated and normalized to gene number, CDS length, and total P-site occupancy.
(C) Mean P-site counts per million were plotted for every codon of the RPS27 CDS. The empty vector is plotted above the x axis, and shKBP10 is plotted below in negative. Proline codons within the first 20 are highlighted.
(D) Translational efficiency (TE) was assessed using ratios of Ribo-seq ribosome footprint RNA and RNA-seq total RNA levels using RiboDiff. The distribution of differences in TE for empty vector versus shFKBP10 was plotted for RP genes (green) and non-RP genes (purple).
(E) Bar plots showing the protein levels of selected RPs (RPS27 and RPS15) measured using western blot assay (normalized over beta-actin), in A549 cells harboring empty vector or shFKBP10.
(F) P-site ribosome dwelling occupancies were calculated in the first 60 nt by normalizing counts for each codon type to total counts and codon frequency for the region. Mean log fold change between before and after FKBP10 knockdown is plotted.
Data are represented as mean ± SEM. Statistical analyses were done using two-tailed unpaired Student's t test (D and E); *$p < 0.05$ and ***$p < 0.001$.
See also Figures S5 and S6 and Tables S4, S5, and S6.

activity is required for the pro-tumoral action of FKBP10. However, FKBP10 is a member of a large family of PPIases. Why are other PPIases not able to compensate for FKBP10 deletion? One possibility is that FKBP10 is unique among these members, as it, and not the others, could have access to the ribosome catalytic center. Hence, a twofold property including its PPIase activity and its location at the ribosome catalytic center could render FKBP10 unique among the members of the PPIase family. Testing this hypothesis will require complex experiments (e.g., co-crystallography assays).

Our data reveal that FKBP10 knockdown before or after tumor onset decreases tumor burden *in vivo*. Nevertheless, FKBP10 knockdown before tumor onset leads to decreased cellular proliferation (with no changes in apoptosis), whereas its downregulation after tumor onset triggers increased cellular apoptosis (with no changes in proliferation). This outcome raises the question of how it is possible that a similar event (i.e., FKBP10 downregulation) leads to two diverse outcomes. We suggest that this apparent conundrum could be due to the different timing at which FKBP10 downregulation is induced (i.e., before versus after tumor onset). For example, FKBP10 downregulation before tumor onset could provide time for compensatory mechanisms protecting tumor cells from undergoing apoptosis while its downregulation after the tumor is induced cannot. Also, this apparent conundrum could be due to the different degree of FKBP10 downregulation. Indeed, the pre-tumor-onset animal model is a haploinsufficient model (in which FKBP10 is downregulated by 50%), whereas the post-tumor-onset animal model is a conditional knockout model (in which FKBP10 is downregulated by 85%). Thus, it is formally possible that a high degree of FKBP10 downregulation is required for apoptosis to be achieved. To directly test these two mutually non-exclusive hypotheses future experiments are required.

Interestingly, we found that FKBP10 is expressed in cancer cells derived from different human cancers (i.e., pancreatic cancer and breast cancer), in which its downregulation showed a strong anti-proliferative effect (Ramadori et al., 2015). In addition, our dataset analyses indicate that FKBP10 expression is a negative prognostic marker in several other malignancies (e.g., stomach adenocarcinoma, intestinal, hepatic, bladder, and renal cancers) (Figure S1C). Thus, these data suggest that FKBP10 might play a role in other types of cancer. Hence, future experiments aimed at assessing the outcome of FKBP10 downregulation in animal models of these cancer types are warranted.

Of note, molecular targets able to selectively and relevantly coordinate protein translation and tumorigenesis are unknown. Identification of such targets could represent an important step towards the development of new anti-cancer therapeutics. Hence, considering that FKBP10 (1) coordinates protein translation and (2) is selectively expressed in cancer lesion, (3) its expression negatively correlates with survival of cancer patients, and (4) its downregulation suppresses cancer growth and cancer stem-like features, we suggest that FKBP10 is an ideal molecular target for developing better therapeutics for NSCLC, a condition for which there is a clear unmet medical need (Ferrer et al., 2018; Pao et al., 2005; Román et al., 2018).

In conclusion, we have identified FKBP10-dependent protein translation elongation as a cancer-specific and cancer-relevant molecular mechanism for NSCLC.

STAR★METHODS

Detailed methods are provided in the online version of this paper and include the following:

- KEY RESOURCES TABLE
- LEAD CONTACT AND MATERIALS AVAILABILITY
- EXPERIMENTAL MODEL AND SUBJECT DETAILS
  - Mice
  - Cell Lines
- METHOD DETAILS
  - Tumorigenesis Induction
  - Fkbp10 Deletion
  - Micro-computed Tomography (Micro-CT) Experiment
  - Tumor Area Assessment
  - Mouse Xenograft Assay
  - Lentiviral Production and Generation of Stable Cell Lines
  - Immunohistochemistry (IHC)
  - Quantitative Real-Time PCR (q-RTPCR)
  - Immunoblotting and Immunoprecipitation
  - Tumorsphere Assay
  - Aldehyde Dehydrogenase (ALDH) Activity Assay and Fluorescence-Activated Cell Sorting (FACS)
  - Measurement of [35S]-Labeled Methionine Incorporation in Cells
  - Polysome Profiling
  - Ribosome Profiling (Ribo-Seq)
  - RNA Sequencing
  - RiboSeq and RNASeq Mapping
  - Ribo-Seq Analysis
  - RNA-Seq Analysis
  - Translational Efficiency (TE) Analysis
- QUANTIFICATION AND STATISTICAL ANALYSIS
- DATA AND CODE AVAILABILITY

SUPPLEMENTAL INFORMATION

Supplemental Information can be found online at https://doi.org/10.1016/j.celrep.2020.02.082.

ACKNOWLEDGMENTS

We thank Mrs. Ariane Widmer for technical support, Drs. Claes Wollheim and Vladimir Katanaev for reading of the manuscript, and Dr. Kury for providing the FKBP10-8FY plasmid. This work was supported by Coordenação de Aperfeiçoamento de Pessoal de Nível Superior (CAPES graduate student fellowship to R.M.I.); the Bo & Kerstin Hjelt Foundation and the Gertrude von Meissner Foundation (research grants to G.R.); the European Commission (Marie Curie Career Integration Grant 320898, European Research Council [ERC] Proof of Concept Grant 899766, and ERC Consolidator Grant 614847); the Geneva Cancer League; the Swiss Cancer League (KLS-3794-02-2016-R); the Juvenile Diabetes Research Foundation (grant 2-SRA-2019-846-S-B); the Louis-Jeantet Foundation; La Fondation pour la Recherche sur le Diabète; the Gertrude von Meissner Foundation; Fondation Pour Recherches Medicales of the University of Geneva to R.C.; and the Swiss National Science Foundation (grants 310030_169966, 310030_184767, and 310030_146533 to R.C.; grant

31003A_172999 to M.A.C.; and professorship PP00P3_163929 to G.K.). We also acknowledge the DiaGen2010 travel grant to R.F.

AUTHOR CONTRIBUTIONS

R.C., M.A.C., and G.R. designed the experiments and supervised the project. G.R., R.M.I., and R.F. performed the *in vivo* experiments. G.R., R.M.I., Z.V., R.F., G.K., E.A., X.B., and A.C. performed the *in vitro* experiments. R.M.I., Z.V., R.F., and O.O.P. performed the ribosome profile experiments. T.B., M.L., and A.S. performed the histological and immuno-histological analyses. G.A., F.B., M.S., and P.B. analyzed data. R.C., G.R., M.A.C., R.M.I., and R.F. wrote the manuscript with the help of all other co-authors.

DECLARATION OF INTERESTS

The authors declare no competing interests.

Received: June 10, 2017
Revised: October 29, 2019
Accepted: February 20, 2020
Published: March 17, 2020

REFERENCES

Alanay, Y., Avaygan, H., Camacho, N., Utine, G.E., Boduroglu, K., Aktas, D., Alikasifoglu, M., Tuncbilek, E., Orhan, D., Bakar, F.T., et al. (2010). Mutations in the gene encoding the RER protein FKBP65 cause autosomal-recessive osteogenesis imperfecta. Am. J. Hum. Genet. *86*, 551–559.

Anderson, J.G., Ramadori, G., Ioris, R.M., Galiè, M., Berglund, E.D., Coate, K.C., Fujikawa, T., Pucciarelli, S., Moreschini, B., Amici, A., et al. (2015). Enhanced insulin sensitivity in skeletal muscle and liver by physiological overexpression of SIRT6. Mol. Metab. *4*, 846–856.

Aras, E., Ramadori, G., Kinouchi, K., Liu, Y., Ioris, R.M., Brenachot, X., Ljubicic, S., Veyrat-Durebex, C., Mannucci, S., Galie, M., et al. (2019). Light entrains diurnal changes in insulin sensitivity of skeletal muscle via ventromedial hypothalamic neurons. Cell Rep. *27*, 2385–2398.e3.

Ashburner, M., Ball, C.A., Blake, J.A., Botstein, D., Butler, H., Cherry, J.M., Davis, A.P., Dolinski, K., Dwight, S.S., Eppig, J.T., et al.; The Gene Ontology Consortium (2000). Gene Ontology: tool for the unification of biology. Nat. Genet. *25*, 25–29.

Bhat, M., Robichaud, N., Hulea, L., Sonenberg, N., Pelletier, J., and Topisirovic, I. (2015). Targeting the translation machinery in cancer. Nat. Rev. Drug Discov. *14*, 261–278.

Boghaert, E.R., Sridharan, L., Khandke, K.M., Armellino, D., Ryan, M.G., Myers, K., Harrop, R., Kunz, A., Hamann, P.R., Marquette, K., et al. (2008). The oncofetal protein, 5T4, is a suitable target for antibody-guided anti-cancer chemotherapy with calicheamicin. Int. J. Oncol. *32*, 221–234.

Burris, H.A., 3rd. (2009). Shortcomings of current therapies for non-small-cell lung cancer: unmet medical needs. Oncogene *28* (*Suppl 1*), S4–S13.

Camidge, D.R., Doebele, R.C., and Kerr, K.M. (2019). Comparing and contrasting predictive biomarkers for immunotherapy and targeted therapy of NSCLC. Nat. Rev. Clin. Oncol. *16*, 341–355.

Carpentino, J.E., Hynes, M.J., Appelman, H.D., Zheng, T., Steindler, D.A., Scott, E.W., and Huang, E.H. (2009). Aldehyde dehydrogenase-expressing colon stem cells contribute to tumorigenesis in the transition from colitis to cancer. Cancer Res. *69*, 8208–8215.

Chen, Y., Terajima, M., Banerjee, P., Guo, H., Liu, X., Yu, J., Yamauchi, M., and Kurie, J.M. (2017). FKBP65-dependent peptidyl-prolyl isomerase activity potentiates the lysyl hydroxylase 2-driven collagen cross-link switch. Sci. Rep. *7*, 46021.

Cheung, A.M., Wan, T.S., Leung, J.C., Chan, L.Y., Huang, H., Kwong, Y.L., Liang, R., and Leung, A.Y. (2007). Aldehyde dehydrogenase activity in leukemic blasts defines a subgroup of acute myeloid leukemia with adverse prognosis and superior NOD/SCID engrafting potential. Leukemia *21*, 1423–1430.

Christiansen, H.E., Schwarze, U., Pyott, S.M., AlSwaid, A., Al Balwi, M., Alrasheed, S., Pepin, M.G., Weis, M.A., Eyre, D.R., and Byers, P.H. (2010). Homozygosity for a missense mutation in SERPINH1, which encodes the collagen chaperone protein HSP47, results in severe recessive osteogenesis imperfecta. Am. J. Hum. Genet. *86*, 389–398.

Cortazar, A.R., Torrano, V., Martín-Martín, N., Caro-Maldonado, A., Camacho, L., Hermanova, I., Guruceaga, E., Lorenzo-Martín, L.F., Caloto, R., Gomis, R.R., et al. (2018). CANCERTOOL: a visualization and representation interface to exploit cancer datasets. Cancer Res. *78*, 6320–6328.

Dontu, G., Abdallah, W.M., Foley, J.M., Jackson, K.W., Clarke, M.F., Kawamura, M.J., and Wicha, M.S. (2003). In vitro propagation and transcriptional profiling of human mammary stem/progenitor cells. Genes Dev. *17*, 1253–1270.

Faller, W.J., Jackson, T.J., Knight, J.R., Ridgway, R.A., Jamieson, T., Karim, S.A., Jones, C., Radulescu, S., Huels, D.J., Myant, K.B., et al. (2015). mTORC1-mediated translational elongation limits intestinal tumour initiation and growth. Nature *517*, 497–500.

Ferrer, I., Zugazagoitia, J., Herbertz, S., John, W., Paz-Ares, L., and Schmid-Bindert, G. (2018). KRAS-mutant non-small cell lung cancer: from biology to therapy. Lung Cancer *124*, 53–64.

Fisher, G.H., Wellen, S.L., Klimstra, D., Lenczowski, J.M., Tichelaar, J.W., Lizak, M.J., Whitsett, J.A., Koretsky, A., and Varmus, H.E. (2001). Induction and apoptotic regression of lung adenocarcinomas by regulation of a K-Ras transgene in the presence and absence of tumor suppressor genes. Genes Dev. *15*, 3249–3262.

Ge, Y., Xu, A., Zhang, M., Xiong, H., Fang, L., Zhang, X., Liu, C., and Wu, S. (2017). FK506 binding protein 10 is overexpressed and promotes renal cell carcinoma. Urol. Int. *98*, 169–176.

The Gene Ontology Consortium (2019). The Gene Ontology resource: 20 years and still GOing strong. Nucleic Acids Res. *47* (*D1*), D330–D338.

Ginestier, C., Hur, M.H., Charafe-Jauffret, E., Monville, F., Dutcher, J., Brown, M., Jacquemier, J., Viens, P., Kleer, C.G., Liu, S., et al. (2007). ALDH1 is a marker of normal and malignant human mammary stem cells and a predictor of poor clinical outcome. Cell Stem Cell *1*, 555–567.

Guan, B.J., Krokowski, D., Majumder, M., Schmotzer, C.L., Kimball, S.R., Merrick, W.C., Koromilas, A.E., and Hatzoglou, M. (2014). Translational control during endoplasmic reticulum stress beyond phosphorylation of the translation initiation factor eIF2α. J. Biol. Chem. *289*, 12593–12611.

Ingolia, N.T., Ghaemmaghami, S., Newman, J.R., and Weissman, J.S. (2009). Genome-wide analysis in vivo of translation with nucleotide resolution using ribosome profiling. Science *324*, 218–223.

Ioris, R.M., Galié, M., Ramadori, G., Anderson, J.G., Charollais, A., Konstantinidou, G., Brenachot, X., Aras, E., Goga, A., Ceglia, N., et al. (2017). SIRT6 suppresses cancer stem-like capacity in tumors with PI3K activation independently of its deacetylase activity. Cell Rep. *18*, 1858–1868.

Ishikawa, Y., Vranka, J., Wirz, J., Nagata, K., and Bächinger, H.P. (2008). The rough endoplasmic reticulum-resident FK506-binding protein FKBP65 is a molecular chaperone that interacts with collagens. J. Biol. Chem. *283*, 31584–31590.

Iwai, Y., Terawaki, S., and Honjo, T. (2005). PD-1 blockade inhibits hematogenous spread of poorly immunogenic tumor cells by enhanced recruitment of effector T cells. Int. Immunol. *17*, 133–144.

Kelley, B.P., Malfait, F., Bonafe, L., Baldridge, D., Homan, E., Symoens, S., Willaert, A., Elcioglu, N., Van Maldergem, L., Verellen-Dumoulin, C., et al. (2011). Mutations in FKBP10 cause recessive osteogenesis imperfecta and Bruck syndrome. J. Bone Miner. Res. *26*, 666–672.

Kim, D., Langmead, B., and Salzberg, S.L. (2015). HISAT: a fast spliced aligner with low memory requirements. Nat. Methods *12*, 357–360.

Konstantinidou, G., Ramadori, G., Torti, F., Kangasniemi, K., Ramirez, R.E., Cai, Y., Behrens, C., Dellinger, M.T., Brekken, R.A., Wistuba, I.I., et al. (2013). RHOA-FAK is a required signaling axis for the maintenance of KRAS-driven lung adenocarcinomas. Cancer Discov. *3*, 444–457.

Langmead, B., and Salzberg, S.L. (2012). Fast gapped-read alignment with Bowtie 2. Nat. Methods *9*, 357–359.

Lapidot, T., Sirard, C., Vormoor, J., Murdoch, B., Hoang, T., Caceres-Cortes, J., Minden, M., Paterson, B., Caligiuri, M.A., and Dick, J.E. (1994). A cell initiating human acute myeloid leukaemia after transplantation into SCID mice. Nature *367*, 645–648.

Lauria, F., Tebaldi, T., Bernabò, P., Groen, E.J.N., Gillingwater, T.H., and Viero, G. (2018). riboWaltz: optimization of ribosome P-site positioning in ribosome profiling data. PLoS Comput. Biol. *14*, e1006169.

Lawrence, D.M., Patterson, C.E., Gales, T.L., D'Orazio, J.L., Vaughn, M.M., and Rall, G.F. (2000). Measles virus spread between neurons requires cell contact but not CD46 expression, syncytium formation, or extracellular virus production. J. Virol. *74*, 1908–1918.

Leach, D.R., Krummel, M.F., and Allison, J.P. (1996). Enhancement of antitumor immunity by CTLA-4 blockade. Science *271*, 1734–1736.

Liang, L., Zhao, K., Zhu, J.H., Chen, G., Qin, X.G., and Chen, J.Q. (2019). Comprehensive evaluation of FKBP10 expression and its prognostic potential in gastric cancer. Oncol. Rep. *42*, 615–628.

Lietman, C.D., Rajagopal, A., Homan, E.P., Munivez, E., Jiang, M.M., Bertin, T.K., Chen, Y., Hicks, J., Weis, M., Eyre, D., et al. (2014). Connective tissue alterations in Fkbp10-/- mice. Hum. Mol. Genet. *23*, 4822–4831.

Liu, B., Han, Y., and Qian, S.B. (2013). Cotranslational response to proteotoxic stress by elongation pausing of ribosomes. Mol. Cell *49*, 453–463.

Loayza-Puch, F., Rooijers, K., Buil, L.C., Zijlstra, J., Oude Vrielink, J.F., Lopes, R., Ugalde, A.P., van Breugel, P., Hofland, I., Wesseling, J., et al. (2016). Tumour-specific proline vulnerability uncovered by differential ribosome codon reading. Nature *530*, 490–494.

Monk, M., and Holding, C. (2001). Human embryonic genes re-expressed in cancer cells. Oncogene *20*, 8085–8091.

Nagy, Á., Lánczky, A., Menyhárt, O., and Győrffy, B. (2018). Validation of miRNA prognostic power in hepatocellular carcinoma using expression data of independent datasets. Sci. Rep. *8*, 9227.

Olesen, S.H., Christensen, L.L., Sørensen, F.B., Cabezón, T., Laurberg, S., Orntoft, T.F., and Birkenkamp-Demtröder, K. (2005). Human FK506 binding protein 65 is associated with colorectal cancer. Mol. Cell. Proteomics *4*, 534–544.

Pao, W., Wang, T.Y., Riely, G.J., Miller, V.A., Pan, Q., Ladanyi, M., Zakowski, M.F., Heelan, R.T., Kris, M.G., and Varmus, H.E. (2005). KRAS mutations and primary resistance of lung adenocarcinomas to gefitinib or erlotinib. PLoS Med. *2*, e17.

Pattabiraman, D.R., and Weinberg, R.A. (2014). Tackling the cancer stem cells—what challenges do they pose? Nat. Rev. Drug Discov. *13*, 497–512.

Patterson, C.E., Schaub, T., Coleman, E.J., and Davis, E.C. (2000). Developmental regulation of FKBP65. An ER-localized extracellular matrix binding-protein. Mol. Biol. Cell *11*, 3925–3935.

Penzo, M., Montanaro, L., Treré, D., and Derenzini, M. (2019). The ribosome biogenesis-cancer connection. Cells *8*, 55.

Ponti, D., Costa, A., Zaffaroni, N., Pratesi, G., Petrangolini, G., Coradini, D., Pilotti, S., Pierotti, M.A., and Daidone, M.G. (2005). Isolation and in vitro propagation of tumorigenic breast cancer cells with stem/progenitor cell properties. Cancer Res. *65*, 5506–5511.

Prost, S., Relouzat, F., Spentchian, M., Ouzegdouh, Y., Saliba, J., Massonnet, G., Beressi, J.P., Verhoeyen, E., Raggueneau, V., Maneglier, B., et al. (2015). Erosion of the chronic myeloid leukaemia stem cell pool by PPARγ agonists. Nature *525*, 380–383.

Quinn, M.C., Wojnarowicz, P.M., Pickett, A., Provencher, D.M., Mes-Masson, A.M., Davis, E.C., and Tonin, P.N. (2013). FKBP10/FKBP65 expression in high-grade ovarian serous carcinoma and its association with patient outcome. Int. J. Oncol. *42*, 912–920.

Ramadori, G., Konstantinidou, G., Venkateswaran, N., Biscotti, T., Morlock, L., Galié, M., Williams, N.S., Luchetti, M., Santinelli, A., Scaglioni, P.P., and Coppari, R. (2015). Diet-induced unresolved ER stress hinders KRAS-driven lung tumorigenesis. Cell Metab. *21*, 117–125.

Ramadori, G., Ljubicic, S., Ricci, S., Mikropoulou, D., Brenachot, X., Veyrat-Durebex, C., Aras, E., Ioris, R.M., Altirriba, J., Malle, E., et al. (2019). S100A9 extends lifespan in insulin deficiency. Nat. Commun. *10*, 3545.

Rasheed, Z.A., Yang, J., Wang, Q., Kowalski, J., Freed, I., Murter, C., Hong, S.M., Koorstra, J.B., Rajeshkumar, N.V., He, X., et al. (2010). Prognostic significance of tumorigenic cells with mesenchymal features in pancreatic adenocarcinoma. J. Natl. Cancer Inst. *102*, 340–351.

Robinson, M.D., McCarthy, D.J., and Smyth, G.K. (2010). edgeR: a Bioconductor package for differential expression analysis of digital gene expression data. Bioinformatics *26*, 139–140.

Román, M., Baraibar, I., López, I., Nadal, E., Rolfo, C., Vicent, S., and Gil-Bazo, I. (2018). KRAS oncogene in non-small cell lung cancer: clinical perspectives on the treatment of an old target. Mol. Cancer *17*, 33.

Ruzankina, Y., Pinzon-Guzman, C., Asare, A., Ong, T., Pontano, L., Cotsarelis, G., Zediak, V.P., Velez, M., Bhandoola, A., and Brown, E.J. (2007). Deletion of the developmentally essential gene ATR in adult mice leads to age-related phenotypes and stem cell loss. Cell Stem Cell *1*, 113–126.

Sahu, N., Dela Cruz, D., Gao, M., Sandoval, W., Haverty, P.M., Liu, J., Stephan, J.P., Haley, B., Classon, M., Hatzivassiliou, G., and Settleman, J. (2016). Proline starvation induces unresolved ER stress and hinders mTORC1-dependent tumorigenesis. Cell Metab. *24*, 753–761.

Son, C.H., Bae, J., Lee, H.R., Yang, K., and Park, Y.S. (2017). Enhancement of antitumor immunity by combination of anti-CTLA-4 antibody and radioimmunotherapy through the suppression of Tregs. Oncol. Lett. *13*, 3781–3786.

Wang, J.C., and Dick, J.E. (2005). Cancer stem cells: lessons from leukemia. Trends Cell Biol. *15*, 494–501.

Wang, D., and Lippard, S.J. (2005). Cellular processing of platinum anticancer drugs. Nat. Rev. Drug Discov. *4*, 307–320.

Wolchok, J. (2018). Putting the immunologic brakes on cancer. Cell *175*, 1452–1454.

Yasumoto, K., Hanagiri, T., and Takenoyama, M. (2009). Lung cancer-associated tumor antigens and the present status of immunotherapy against non-small-cell lung cancer. Gen. Thorac. Cardiovasc. Surg. *57*, 449–457.

Yong, K.J., Li, A., Ou, W.B., Hong, C.K., Zhao, W., Wang, F., Tatetsu, H., Yan, B., Qi, L., Fletcher, J.A., et al. (2016). Targeting SALL4 by entinostat in lung cancer. Oncotarget *7*, 75425–75440.

Zeissig, Y., Petersen, B.S., Milutinovic, S., Bosse, E., Mayr, G., Peuker, K., Hartwig, J., Keller, A., Kohl, M., Laass, M.W., et al. (2015). XIAP variants in male Crohn's disease. Gut *64*, 66–76.

Zhong, Y., Karaletsos, T., Drewe, P., Sreedharan, V.T., Kuo, D., Singh, K., Wendel, H.G., and Rätsch, G. (2017). RiboDiff: detecting changes of mRNA translation efficiency from ribosome footprints. Bioinformatics *33*, 139–141.

Zugazagoitia, J., Guedes, C., Ponce, S., Ferrer, I., Molina-Pinelo, S., and Paz-Ares, L. (2016). Current challenges in cancer treatment. Clin. Ther. *38*, 1551–1566.

STAR★METHODS

KEY RESOURCES TABLE

REAGENT or RESOURCE	SOURCE	IDENTIFIER
Antibodies		
Rabbit Polyclonal FKBP65	ProteinTech	Cat#12172-1-AP; RRID:AB_2102550
Rabbit Monoclonal Phospho-eIF2α (Ser51)	Cell signaling	Cat#3398; RRID:AB_2096481
Rabbit Monoclonal eIF2α (D7D3)	Cell signaling	Cat# 5324; RRID:AB_10692650
Mouse Monoclonal β-Actin (8H10D10)	Cell signaling	Cat#3700; RRID:AB_2242334
Rabbit Monoclonal GAPDH (14C10)	Cell signaling	Cat#2118; RRID:AB_561053
Rabbit Polyclonal RPS27	ProteinTech	Cat#15355-1-AP; RRID:AB_2180509
Rabbit Polyclonal RPS15	ProteinTech	Cat#14957-1-AP; RRID:AB_2180163
Mouse Monoclonal β-Tubulin	Merck	Cat#05-661; RRID:AB_309885
Rabbit Monoclonal Ki67 (D3B5)	Cell signaling	Cat#12202; RRID:AB_2620142
Rabbit Monoclonal Cleaved Caspase-3 (D3E9)	Cell signaling	Cat#9579; RRID:AB_10897512
Rabbit Monoclonal S6 Ribosomal Protein (5G10)	Cell signaling	Cat#2217S; RRID:AB_331355
Purified Mouse Anti-FKBP65	BD Transduction Laboratories	Cat#610648; RRID:AB_397975
IRDye 680RD Goat anti-Mouse IgG Secondary Antibody	LI-COR Biosciences	Cat#926-68070; RRID:AB_10956588
IRDye 800CW Goat anti-Rabbit IgG Secondary Antibody	LI-COR Biosciences	Cat#926-32211; RRID:AB_621843
Biotinylated Goat Anti-Rabbit IgG Antibody	Vector Laboratories	Cat#BA-1000; RRID:AB_2313606
Biological Samples		
Tissue array	Biomax	Cat#LC1921 D137
Chemicals, Peptides, and Recombinant Proteins		
Penicillin-streptomycin	GIBCO	Cat#15140
FBS	Pan Biotech	Cat#P30-3302
MammoCult Medium	STEMCELL Technologies	Cat#05620
MethoCult H4100	STEMCELL Technologies	Cat#04100
Phosphatase and protease inhibitors	Sigma	Cat# P2714-1BTL
Tamoxifen	Sigma	Cat#10540-29-1
Doxycycline	Clontech	Cat#P2250
Heparin Solution 0.2%	STEMCELL Technologies	Cat#07980
Hydrocortisone	STEMCELL Technologies	Cat#74144
TransIT-293 transfection reagent	Mirus	Cat#MIR 2705
Puromycin	GIBCO	Cat# A1113803
Blasticidine	GIBCO	Cat#A1113909
Cycloheximide	Sigma	Cat#66-81-9
Superscript II	Invitrogen	Cat#18064014
SYBR Green PCR master mix	Applied Biosystem	Cat#4344463
RNase I	Epicenter	Cat#N6901K
Protein A-Agarose	Santa Cruz Biotechnology	Cat#sc2001
Scintillation fluid	Amersham Biosciences	Cat#NOCS 104
EnVision FLEX Target Retrieval Solution low pH	Dako	Cat#GV805
EnVision FLEX /HRP	Dako	Cat#GV925
Critical Commercial Assays		
Aldefluor kit	STEMCELL Technologies	Cat#01700
Monarch Total RNA miniprep kit	NEB	Cat#T2010S
RNeasy Mini Kit	QIAGEN	Cat#74104

(*Continued on next page*)

Continued

REAGENT or RESOURCE	SOURCE	IDENTIFIER
Deposited Data		
Ribo-sequencing data	This paper	GEO: GSE129654
RNA-sequencing data	This paper	GEO: GSE129654
Experimental Models: Cell Lines		
Human: A549 cells	ATCC	Cat#CCL-18
Human: H1650 cells	ATCC	Cat#CRL-5883
Human: DLD-1 cells	X-MAN	Cat#HD PAR-086
Human: HT-29 cells	ATCC	Cat#HTB-38
Human: MCF10DCIS cells	ExPASy	MCF10DCIS.com (RRID:CVCL_5552)
Human: MDA-MB-231 cells	ATCC	Cat#HTB-26
Human: 293T	ATCC	Cat#CRL-3216
Experimental Models: Organisms/Strains		
Mouse: Tet-o-K-Ras^{G12D}	Ramadori et al., 2015	N/A
Mouse: CCSP-rtTA	Ramadori et al., 2015	N/A
Mouse: Fkbp10$^{+/-}$ (Fkbp10$^{tm2a(EUCOMM)Wtsi}$)	European Mouse Mutant Archive	Cat#07823
Mouse: Fkbp10$^{loxP/loxP}$	This paper	N/A
Mouse: Ubi-Cre: B6;129S-Tg(UBC-Cre/ERT2)1Ejb/J	The Jackson Laboratory	Cat#007001
Mouse: NOD/SCID: NOD.CB17-Prkdc^{scid}/J	Charles River Laboratories	Cat#001303
Oligonucleotides		
β-Actin forward: 5′-AGGCACCAGGGC GTGAT-3′	Microsynth	N/A
β-Actin reverse: 5′-GCCCACATA GGAATCCTTCTGAC-3′	Microsynth	N/A
RLP38 forward: 5′-CCCGACGAAAGG ATGCCAAAT-3′	Microsynth	N/A
RLP38 reverse: 5′-TGACCAGGGTGT AAAGGTATCTG-3′	Microsynth	N/A
RPS6 forward: 5′-TGGACGATGAAC GCAAACTTC-3′	Microsynth	N/A
RPS6 reverse: 5′-TTCGGACCACAT AACCCTTCC-3′	Microsynth	N/A
RPS27 forward: 5′-ATGCCTCTCGCAAAGGATCTC-3′	Microsynth	N/A
RPS27 reverse: 5′-TGAAGTAGGAATTGGGGCTCT-3′	Microsynth	N/A
RPS13 forward: 5′-TCCCAGTCGGCTTTACCCTAT-3′	Microsynth	N/A
RPS13 reverse: 5′-CAGGATTACACCGATCTGTGAAG-3′	Microsynth	N/A
Recombinant DNA		
pLKO lentiviral containing shRNA targeting FKBP10	Open Biosystems	Cat#TCRN0000053928 Cat#TCRN0000053929
pLVX modified lentivirus containing FKBP10 wild type	Chen et al., 2017	N/A
pLVX modified lentivirus containing FKBP10-FY8	Chen et al., 2017	N/A
pMD2G (VSV-G protein)	Addgene	Cat#12259
pCMV dR8.74	Addgene	Cat#22036
Software and Algorithms		
FlowJo version 10.6.1	FlowJo	https://www.flowjo.com/
Zen 2	Zeiss	https://www.zeiss.com/
Analyze 12.0	AnayzeDirect	https://analyzedirect.com/
MetaXpress version 5.1.0.41	Molecular Devices	https://www.moleculardevices.com/
Prism 8.0.1	GraphPad	https://www.graphpad.com/
R version 3.3.2	R	www.r-project.org
riboWaltz	Lauria et al., 2018	N/A
edgeR	Robinson et al., 2010	N/A
RiboDiff	Zhong et al., 2017	N/A

LEAD CONTACT AND MATERIALS AVAILABILITY

Further information and requests for resources and reagents should be directed to and will be fulfilled by the Lead Contact, Roberto Coppari (roberto.coppari@unige.ch).

This study did not generate new unique reagents.

EXPERIMENTAL MODEL AND SUBJECT DETAILS

Mice

The following mice were used in this study: *Kras^{G12D}; Fkbp10$^{+/-}$*: Tumorigenesis was induced in littermates *CC10-rtTA/Tet-o-K-Ras^{G12D}* bi-transgenic mice (hereafter indicated as *Kras^{G12D}* mice) and *Kras^{G12D}* mice heterozygous for a FKBP10 null allele (Ingolia et al.) (*Kras^{G12D}*; *Fkbp10$^{+/-}$*) as previously described (Fisher et al., 2001). Male mice were used for this experiment. *Kras^{G12D}; Fkbp10$^{loxP/loxP}$; Ubi-Cre*: This animal model was generated by breeding mice bearing the *Tet-op-Kras* (Konstantinidou et al., 2013) and heterozygous for the lox-P-flanked *Fkbp10* loci (Fisher et al., 2001) with mice bearing the *CCSP-rtTA* (Konstantinidou et al., 2013) and the *Ubi*-Cre (Ruzankina et al., 2007) alleles and heterozygous for the lox-P-flanked *Fkbp10* loci (Fisher et al., 2001). From their offspring, this animal model bears 5 different alleles: *Tet-op-Kras* (Konstantinidou et al., 2013)*; CCSP-rtTA* (Konstantinidou et al., 2013); two lox-P-flanked *Fkbp10* loci (Fisher et al., 2001); and the *Ubi*-Cre (Ruzankina et al., 2007) allele. Female mice were used for this experiment. Non-obese diabetic/severe combined immunodeficient (NOD/SCID): Mice were housed in a pathogen-free animal facility. Female mice were used for this experiment.

All mice were maintained with standard rodent chow diet and water available *ad libitum*, under a 12 h light/dark cycle at constant temperature and humidity. Care of mice at University of Geneva was within the procedures approved by animal care and experimentation authorities of the Canton of Geneva, Switzerland (animal protocol numbers GE/78/18 and GE/83/18).

Cell Lines

The following cancer cell lines were used: A549 and H1650 (lung cancer cell lines), DLD-1 and HT-29 (colorectal cancer cell lines), MCF10DCIS and MDA-MB-231 (breast cancer cell lines). Cells were grown in RPMI media containing 10% FBS (Pan Biotech), Penicillin (100 I.U./mL), and Streptomycin (100 μg/mL) (GIBCO) at 37°C in humidified atmosphere with 5% CO2.

METHOD DETAILS

Tumorigenesis Induction

Tumorigenesis was induced in 8-weeks old mice (*Kras^{G12D}* control and *Kras^{G12D}; Fkbp10$^{+/-}$; Kras^{G12D}; Fkbp10$^{loxP/loxP}$* and *Kras^{G12D}; Fkbp10$^{loxP/loxP}$; Ubi-Cre*) by drinking water supplemented with doxycycline (Clontech) at concentration of 200 μg/mL for the length of time indicated in the figure legends.

Fkbp10 Deletion

Tamoxifen (30mg/ml) (Sigma) was mixed with corn oil and 100μl tamoxifen/corn oil solution was administered by intraperitoneal injection in each *Kras^{G12D}*; *Fkbp10$^{loxP/loxP}$*; *Ubi-Cre* and *Kras^{G12D}*; *Fkbp10$^{loxP/loxP}$* mouse once every 24 hours for a total of 5 consecutive days.

Micro-computed Tomography (Micro-CT) Experiment

Mice were anaesthetized with 5% isoflurane and transferred into a micro-CT Quantum GX (Perkin Elmer, Waltham, MA, USA), where anesthesia was maintained by constant exposure to 1.5% isoflurane. Mice were scanned at 90 kV and 80 mA over 360° using the retrospective dual phase (expiration and inspiration) respiratory gating protocol of the micro-CT with a field of view of 36 mm and a resolution of 72 μm (voxel size). Analyses were performed on the expiration phase scan by Analyze 12.0 software.

Tumor Area Assessment

Mouse lungs and tumors were fixed in 4% paraformaldehyde (PFA) overnight at 4°C and cut in 5-μm-thick sections using a cryostat. Lung sections were stained with Hematoxylin and eosin (H&E). Slides were scanned by Zeiss Axio-scanZ1, and tumor area was assessed by digital quantification of the area occupied by tumors in the left lobe compared to unaffected tissue using Zen2 software (Zeissig et al., 2015).

Mouse Xenograft Assay

Cells were trypsinized, suspended in PBS, and injected subcutaneously into the flank of 8-week-old NOD/SCID mice. A549 and H1650 cells were injected at the following concentrations: $1x10^4$, $5x10^4$ and $1x10^5$. Mice were checked every 3 days for tumor appearance.

Lentiviral Production and Generation of Stable Cell Lines

For the knockdown of FKBP10, cancer cells (A549, H1650, DLD-1, HT-29, MCF10DCIS and MDA-MB-231) were infected with lentiviruses carrying pLKO (control vector), or pLKO shFKBP10 (Open Biosystem). Cells were selected with puromycin to generate stably transfected cells.

For FKBP10 overexpression, cancer cells (DLD-1 and MDA-MB-231) were infected with pLVX modified lentiviruses expressing FKBP10-WT, FKBP10-8FY or empty (control vector) [FKBP10-8FY plasmid was kindly provided by Prof. Kurie JM, The University of Texas, and produced as previously described (Chen et al., 2017)]. This recombinant lentivirus was produced as mentioned previously. Cells were selected with blasticidin to generate stably transfected cells.

The recombinant lentivirus was produced by transfecting 293T cells, using TransIT-293 transfection reagent (Mirus), with pMD2G (VSV-G protein), pCMV dR8.74 (lentivirus packaging vector) and lentiviral constructs.

Immunohistochemistry (IHC)

Mouse lungs and tumors were fixed in 4% PFA overnight at 4°C and cut in 5-μm-thick sections using a cryostat. Sections were incubated with primary antibodies overnight at room temperature. Primary antibodies used were: Ki67 (Cell Signaling; dilution 1:400) and cleaved Caspase-3 (Cell Signaling; dilution 1:300). Secondary antibody used was Biotinylated Goat Anti-Rabbit IgG Antibody (Vector Laboratories; dilution 1:100 for Ki67 and 1:1000 for cleaved Caspase-3). Hematoxylin was used as counterstaining in IHC for both markers. In order to quantify the percentage of Ki67 and cleaved Caspase-3 positive cells, a total of 200 cells were scored/slide for at least 3 replicates.

To determine FKBP10 expression in human paraffin embedded lung samples (Biomax), we used the following procedure. Sections were deparaffinized and the detection of antigens has occurred in automated manner with Dako PT Link using EnVision FLEX Target Retrieval Solution low pH (50X) (Dako) at temperature of 98°C. After 70 minutes of treatment, sections were treated with 3% hydrogen peroxide and incubated for 30 minutes with unconjugated anti-mouse IgG at room temperature. Subsequently, sections were incubated for 1 hour at room temperature with mouse Anti-FKBP10 antibody (1:750, BD Transduction Laboratories). The staining was completed using EnVision FLEX /HRP (Dako), as detection system; 3,3-diaminobenzidine-hydrogen peroxide was used as chromogen. Then, slides were counterstained with Meyer's hematoxylin for 1 minute, dehydrated in a graded series of alcohol, treated with xylene, and coverslipped. Immunohistochemical staining was semiquantitatively assessed by considering the "percentage of positive tumor cells" (range 0%–100%).

Quantitative Real-Time PCR (q-RTPCR)

RNA was extracted using RNeasy Mini Kit (QIAGEN). Complementary DNA was generated by Superscript II (Invitrogen) and used with SYBR Green PCR master mix (Applied Biosystem) for q-RTPCR analysis. mRNA contents were normalized to β-Actin mRNA levels. All assays were performed using an Applied Biosystems Quant Studio 5 Real-Time PCR System. For each mRNA assessment, q-RTPCR analyses were repeated 3 times as previously done (Anderson et al., 2015; Aras et al., 2019; Ramadori et al., 2019).

Immunoblotting and Immunoprecipitation

Immunoblots were performed according to standard procedures in RIPA buffer (150 mM NaCl, 10 mM Tris pH 7.5, 1% NP40, 1% Deoxycholate, 0.1% SDS) and supplemented with phosphatase and protease inhibitors (Sigma). Samples were resolved by SDS-PAGE and finally transferred to a nitrocellulose membrane by electroblotting. The following primary antibodies were used: p-eIF2α and eIF2α (Cell signaling), β-Actin (Cell signaling), GAPDH (Cell signaling), β-Tubulin (Merck), FKBP10 (ProteinTech), S6 Ribosomal Protein (Cell signaling), RPS27 and RPS15 (ProteinTech). The following secondary antibodies were used: Goat anti-Mouse IgG and Goat anti-Rabbit IgG (LI-COR Biosciences).

For immunoprecipitation with FKBP10 antibody (1μg) we used 500μg of whole protein lysate from A549 cells and we followed the protein A-agarose immunoprecipitation reagents and protocol from Santa Cruz Biotechnology.

Tumorsphere Assay

Tumorsphere formation was induced in ultralow-adherent 6-well plates. Cancer cells (A549, H1650, DLD-1, HT-29, MCF10DCIS and MDA-MB-231) were plated at a density of 5,000 cells per well in triplicate in a 6-well plate in a 1% methylcellulose containing media (MammoCult supplemented with MethoCult media, STEMCELL Technologies). Tumorsphere formation was quantified 7 days after plating, by MetaXpress version 5.1.0.41. Spheres with a diameter equal or higher than 50 μm were deemed tumorspheres. Experiments were repeated three times for each condition.

Aldehyde Dehydrogenase (ALDH) Activity Assay and Fluorescence-Activated Cell Sorting (FACS)

ALDH activity was measured in cancer cells using the Aldefluor kit (STEMCELL Technologies) following the manufacturer's protocol. A549, H1650 and DLD-1 cancer cells (at concentration of $1x10^6$) were incubated with Aldefluor reagent and N,N-diethylaminobenzaldehyde (DEAB; represented in blue) or Aldefluor reagent only (represented in red). After 40 minutes of incubation period, cells were analyzed by flow cytometry, following the supplier's recommendation, and results were generated using FlowJo software. Values mentioned along with the graphs indicate percentage of cells with high ALDH activity. Experiments were repeated twice for each cell line.

A549 cells with high or low ALDH activity were isolated by FACS, and tumorsphere assay was performed in these cells.

Measurement of [35S]-Labeled Methionine Incorporation in Cells

Equally grown (60% confluency) A549 cells harboring empty vector or shFKBP10 were incubated with 300 μCi [35S]-labeled methionine for 30 minutes and were extracted in lysis buffer [10mM HEPES, 100mM KCl, 5mM $MgCl_2$, 100 μg/ml cycloheximide and 2% of Triton X-100 (ph 7.4)]. Protein extract was trichloroacetic acid (TCA) precipitated with 300 μl of ice-cold 25% TCA containing 2% of casamino acids for 30 minutes on ice. The precipitate was collected by vacuum filtering of 250 μl of the TCA reaction mix on Whatman GF/A glass fiber filters. Amino acids were removed by rinsing the filter 3 times with 1 mL of ice-cold 5% TCA. For determination of [35S]-labeled methionine incorporation into translation products, the filter was placed into scintillation fluid (Amersham Biosciences) and counted in a Wallac 1409 liquid scintillation counter.

Polysome Profiling

A549 cells were treated for 30 minutes with 100 μg/ml cycloheximide prior to harvesting, then were scraped at 4°C and lysed in lysis buffer [10mM HEPES, 100mM KCl, 5mM $MgCl_2$, 100 μg/ml cycloheximide and 2% of Triton X-100 (ph 7.4)]. Cleared lysates were loaded on sucrose gradients and fractionated by ultracentrifugation. Fractionation was monitored by the continuous reading of OD_{254} values.

Ribosome Profiling (Ribo-Seq)

Ribo-Seq was performed on A549 cells harboring empty vector or shFKBP10 in biological duplicates as described previously (Ingolia et al., 2009). Briefly, cells were grown to reach 70% confluence, and treated for 1 minute with 100 μg/ml cycloheximide at 37°C. Cells were lysed in a lysis buffer (20 mM Tris, pH 7.4, 150 mM NaCl, 5 mM MgCl2, 1% Triton X-100, 25 U/ml Turbo DNase I, 1mM DTT, 100 μg/ml cycloheximide, and Protease inhibitors). 0.4 mL of total extracts containing 150 μg of total RNA were treated with RNase I (Epicenter) (0.005U/1 μg of RNA), and monosomes were isolated after separation on a 10%–50% sucrose gradient. Libraries were made from the ribosome-protected fragments and subjected to deep sequencing.

RNA Sequencing

An aliquot of the extract used for ribosome profiling was kept for total RNA sequencing. RNA was extracted using the Monarch Total RNA miniprep kit (NEB) and sent for library preparation and sequencing to Fasteris.

RiboSeq and RNASeq Mapping

For the Ribo-Seq samples, all fastq files were adaptor stripped using cutadapt. Only trimmed reads were retained, with a minimum length of 20 and a quality cutoff of 2 (parameters: -a CTGTAGGCACCATCAATAGATCGGAAGAGCACACGTCTGAACTCCAGTCAC–trimmed-only–minimum-length = 20–quality-cutoff = 2). Histograms were produced of ribosome footprint lengths and reads were retained if the trimmed size was between 32 and 35.

For all Ribo-Seq and RNA-Seq samples, reads were mapped, using default parameters, with HISAT2 (Kim et al., 2015) to GRCh38, using Ensembl release 84 gtf for transcript definitions. Only primary alignments were retained and reads were removed if they mapped to rRNA, tRNA and pseudogenes according to hg38 RepeatMasker definitions from UCSC. A full set of transcript and CDS sequences for Ensembl release 84 was then established. Only canonical transcripts [defined as those with the longest coding sequences (CDS) for each gene] were retained with their corresponding CDS. Reads were then mapped to the canonical transcriptome with bowtie2 (Langmead and Salzberg, 2012), using default parameters.

Ribo-Seq Analysis

The P-site position of each read was predicted by riboWaltz (Lauria et al., 2018) and confirmed by inspection (reads were shifted 13 bases from the 5′ end). Counts were made by aggregating P-sites overlapping with the CDS and P-sites Per Kilobase Million (PPKMs) were then generated through normalizing by CDS length and total counts for the sample. Differential expression was performed between empty vector and shFKBP10 duplicates using edgeR (Robinson et al., 2010) on default settings. Transcripts were only kept in the analysis if they had a CPM > 1 in both duplicates for either empty vector or shFKBP10 or both.

For further analysis transcripts were filtered if their CDS length was not a multiple of three and if they did not begin with a standard start codon (Lawrence et al., 2000) and end with a standard stop codon (UAG, UGA, UAA). This left 19364 remaining from the original 20346 transcripts. For various groups of genes, summary profile plots were made for start and stop sites by summing p-sites falling into each codon in the first and last 201 bases of each CDS in the gene group with a length greater than 402 bases (a flanking region of 30 bases up and downstream was also included for context). Scaled plots summarizing the p-site depth profile over all genes for the whole CDS was plotted by splitting every CDS in the gene group into 100 equal bins and aggregating the number of p-sites falling in each.

RNA-Seq Analysis

Counts were made by aggregating any reads overlapping with the CDS and RPKMs were then generated through normalizing by CDS length and total counts for the sample. Differential expression was performed as with the Ribo-Seq.

Translational Efficiency (TE) Analysis

TE was assessed using RiboDiff (Zhong et al., 2017) with default parameters with the same Ribo-Seq and RNA-Seq samples as input, using the same expression pre-filters as the edgeR differential expression analysis.

QUANTIFICATION AND STATISTICAL ANALYSIS

A two-tailed unpaired Student's t test was used for comparisons between two groups. A log-rank (Mantel–Cox) was used to compare survival curves. All statistical tests were performed with GraphPad Prism software 8.0.1, or R version 3.3.2. $p < 0.05$ was considered statistically significant. Data are reported as mean ± SEM. No statistical methods were used to predetermine sample size.

DATA AND CODE AVAILABILITY

The accession number for our data is GEO: GSE129654.

The data supporting the findings of the current study that have not been deposited in a public repository are available from the corresponding author upon request.